PHYSICAL REVIEW B **93**, 224108 (2016)

Disjoining potential and grain boundary premelting in binary alloys

J. Hickman and Y. Mishin

Department of Physics and Astronomy, MSN 3F3, George Mason University, Fairfax, Virginia 22030, USA

(Received 27 January 2016; revised manuscript received 4 April 2016; published 27 June 2016)

Many grain boundaries (GBs) in crystalline materials develop highly disordered, liquidlike structures at high temperatures. In alloys, this premelting effect can be fueled by solute segregation and can occur at lower temperatures than in single-component systems. A premelted GB can be modeled by a thin liquid layer located between two solid-liquid interfaces interacting by a disjoining potential. We propose a single analytical form of the disjoining potential describing repulsive, attractive, and intermediate interactions. The potential predicts a variety of premelting scenarios, including thin-to-thick phase transitions. The potential is verified by atomistic computer simulations of premelting in three different GBs in Cu-Ag alloys employing a Monte Carlo technique with an embedded atom potential. The disjoining potential has been extracted from the simulations by analyzing GB width fluctuations. The simulations confirm all shapes of the disjoining potential predicted by the analytical model. One of the GBs was found to switch back and forth between two (thin and thick) states, confirming the existence of thin-to-thick phase transformations in this system. The proposed disjoining potential also predicts the possibility of a cascade of thin-to-thick transitions caused by compositional oscillations (patterning) near solid-liquid interfaces.

DOI: 10.1103/PhysRevB.93.224108

I. INTRODUCTION

A typical grain boundary (GB) in a polycrystalline material has an atomically ordered structure at low temperatures but becomes increasingly disordered as temperature approaches the bulk melting point T_m [1,2]. Very near T_m, many GBs develop liquidlike structures and become wider, often turning into a liquid film. The formation of equilibrium liquidlike GB structures near T_m is referred to as GB *premelting*. Premelting can drastically change GB properties, which in turn can impact properties of the material. The phenomenon of GB premelting is also relevant to grain coalescence during solidification of crystalline materials. As differently oriented crystallites growing from the melt merge together during late stages of solidification, they are separated by a layer of the liquid phase bounded by two solid-liquid interfaces. Depending on the nature of interactions between these interfaces, they can close the liquid gap and create a relatively ordered GB structure, or retain a thin (on the order of a nm) liquid layer, forming a premelted GB. Depending on this, the solidified material can exhibit significantly different properties. Despite many years of research, fundamental understanding of the GB premelting effect remains very incomplete.

Direct experimental information about GB premelting is very limited [1,3–7]. Most experimental studies report indirect evidence based on unusual behavior of GB diffusion, mobility, sliding resistance, contact angles or other GB properties [1,7–13]. The phenomenon has been studied by several computational approaches, such as molecular dynamics (MD) [14–25] and Monte Carlo (MC) [26–28] simulations, phase-field modeling [29–33], and more recently by the phase field crystal method [34–40]. A number of possible premelting scenarios were found in the simulations. These ranged from continuous premelting as the temperature approached T_m from below to a thin-to-thick transition below T_m followed by abrupt melting of the entire material at some temperature above T_m.

On the theoretical side, the simplest and most productive model of GB premelting is one that represents the GB by a uniform liquid layer between two solid-liquid interfaces interacting by a thermodynamic potential $\Psi(w)$ depending on the GB width w [41,42]. This model [41] and its subsequent detailed analysis [42,43] were transferred from the theory of wetting of substrates by thin liquid films, in which the wetting behavior depends on the interaction potential between the two interfaces. This model is capable of predicting a number of GB premelting scenarios, depending on the form of the interaction potential. In this paper we refer to this model as the "liquid layer model" of GB premelting.[1] In addition to simplicity, the advantage of this model is that it puts the GB premelting effect in the context of phase transitions theory and critical phenomena [43,45].

The focus of this paper is on GB premelting in binary alloys. This case is more complex and less studied than premelting in single-component systems. Rappaz *et al.* [44] performed multiphase-field simulations of a binary alloy system in the context of late-stage solidification. The emergence of "dry" or "wet" GBs observed in their simulations was explained by different solid-liquid interaction potentials $\Psi(w)$. The latter were modeled by exponential functions $\Psi(w) = C\exp(-w/\delta)$, which could be made repulsive or attractive by choosing the sign of C. Rappaz *et al.* [44] related their solid-liquid interaction potential to the disjoining effect known from the field of thin liquid films. Following their paper, the interaction potential $\Psi(w)$ employed in GB premelting models came to be called the "disjoining potential." Tang *et al.* [31] developed a phase-field model of GB premelting in binary systems and analyzed possible premelting behaviors

---

[1] Rappaz *et al.* [44] refer to this model as the "sharp interface model" since the solid-liquid interfaces are treated as sharp. We find this term somewhat ambiguous since it might suggest that the entire GB is treated as a sharp interface as it is done in many other theories. The term "liquid layer model" avoids this potential confusion and, we believe, better represents the main idea.

in an abstract eutectic system A–B. GB premelting was also studied [32] by a multiphase-field method with realistic model parameters reproducing the eutectic Cu-Ag system. This study revealed that the disjoining potential can have a variety of shapes intermediate between purely repulsive and purely attractive. The simulations have demonstrated that, under certain conditions, first-order thin-to-thick GB phase transitions can occur near the solidus line. Such transitions can be represented by a transition line on the Cu-Ag phase diagram starting at a GB prewetting point and ending at a critical point near the melting point of pure Cu. A similar multiphase-field model was analyzed by Wang *et al.* [33], who additionally developed an analytical approach to calculations of interaction forces between solid-liquid interfaces. Although their work was primarily focused on a single-component system, they did consider the case of a dilute binary alloy and were able to reproduce the thin-to-thick transition. On the other hand, Rowan [38] performed phase field crystal simulations of GB premelting in binary alloys and did not see such transitions. The disjoining potentials extracted from her simulations were either purely repulsive or purely attractive.

As far as atomistic simulations are concerned, the MD timescale is too short to reach chemical equilibrium with today's computer capabilities. Consequently, MC remains the only feasible approach to simulate binary systems [2]. Williams *et al.* [28] applied the semigrand canonical MC method with an embedded atom potential to study premelting in a high-energy $\Sigma 5$ GB in Cu Ag alloys. It was found that Ag segregation strongly favors GB premelting, which commences at temperatures significantly lower than in pure Cu. As the chemical composition of the grains approached the solidus line from below, the boundary developed a relatively thick layer of the liquid solution whose composition approached the liquidus composition on the phase diagram. Because of the statistical scatter of the data, it was not possible in that work to detect thin-to-thick transitions or extract the disjoining potential.

In this paper, we revisit the Cu-Ag system [28] by more accurate and systematic atomistic simulations. Three different GBs are included in order to probe the effect of GB energy. The disjoining potential has been calculated for all three boundaries by analyzing their width fluctuations. Depending on the chemical composition, the boundaries exhibit repulsive, attractive or intermediate cases of the disjoining potential. An analytical form of disjoining potential is proposed that describes all these cases. Among a number of different premelting scenarios predicted by this potential, the simulations do reveal the thin-to-thick transition that has not been reported in atomistic simulations previously.

In Sec. II of the paper, we discuss different forms of disjoining potentials and propose a new analytical form. We also derive expressions for the equilibrium disjoining pressure near a solidus line, which is one of the ingredients of the liquid layer model. To enable calculations of the disjoining potential from simulation data, we present an equation relating the disjoining potential to equilibrium fluctuations of the GB width in a binary system. After describing our simulation methodology in Sec. III, we report the results for GB premelting in pure Cu (Sec. IV A) and Cu-Ag alloys (Sec. IV B). For completeness, we also apply the thermodynamic integration method to independently compute GB free energies as functions of temperature and/or grain composition. Extrapolation of the computed free energies to the premelting region allows us to validate the disjoining potential calculations and, by extension, the liquid-layer model itself. In Sec. V, we summarize our findings and draw conclusions.

II. THEORY

A. The liquid layer model of grain boundary premelting

Consider a chemically closed binary system containing a liquid layer between two solid regions [Fig. 1(a)]. The cross-section of the system is fixed once and for all. We will assume that the system always remains in thermal equilibrium with a thermostat at a given temperature T. Calculations that do not take thermal equilibrium for granted and solve the problem in terms of energy and entropy can be found in Ref. [46]. The present derivation is simpler and more adapted to the context of atomistic simulations reported later in the paper.

Before discussing the solid-liquid equilibrium, we need to specify thermodynamic properties of the individual bulk phases. The solid (S) and liquid (L) phases are described by the equations of state

$$F_L(T,N_L,N_{2L},V_L), \tag{1}$$

$$F_S(T,N_S,N_{2S},V_S), \tag{2}$$

where F is Helmholtz free energy, N total number of atoms in the phase, N_2 the number of solute atoms (component 2), and V is volume. The derivatives of the free energy are $\partial F_L/\partial N_L = \varphi_L$, $\partial F_S/\partial N_S = \varphi_S$, $\partial F_L/\partial N_{2L} = \mu_2 - \mu_1 \equiv \Delta\mu$, $\partial F_S/\partial N_{2S} = M$, $\partial F_L/\partial V_L = -p_L$, and $\partial F_S/\partial V_S = \sigma_{zz}$, where μ_1 and μ_2 are the chemical potentials in the liquid phase, M is the diffusion potential [47] of the solute relative to the solvent in the solid phase, p_L is pressure in the liquid, and σ_{zz} is the stress component normal to the interfaces. The functions φ_L and φ_S are thermodynamic potentials of the phases (per atom) that will be used below.

Applying the Euler theorem to the homogeneous first degree functions (1) and (2), we obtain

$$F_L - (\Delta\mu)N_{2L} + p_L V_L = N_L\varphi_L,$$
$$F_S - MN_{2S} - \sigma_{zz}V_S = N_S\varphi_S.$$

The left-hand sides are Legendre transforms of the free energy with respect to N_2 and V. Accordingly, φ_L and φ_S are functions of the variables conjugate to N_2 and V:

$$\varphi_L = \varphi_L(T,\Delta\mu,p_L),$$
$$\varphi_S = \varphi_S(T,M,\sigma_{zz}),$$

with the derivatives $\partial\varphi_L/\partial\Delta\mu = -c_L$, $\partial\varphi_S/\partial M = -c_S$, $\partial\varphi_L/\partial p_L = v_L$ and $\partial\varphi_S/\partial\sigma_{zz} = -v_S$, where $c_L = N_{2L}/N_L$ and $c_S = N_{2S}/N_S$ are solute concentrations (atomic fractions) in the phases and v_L and v_S are the respective atomic volumes.

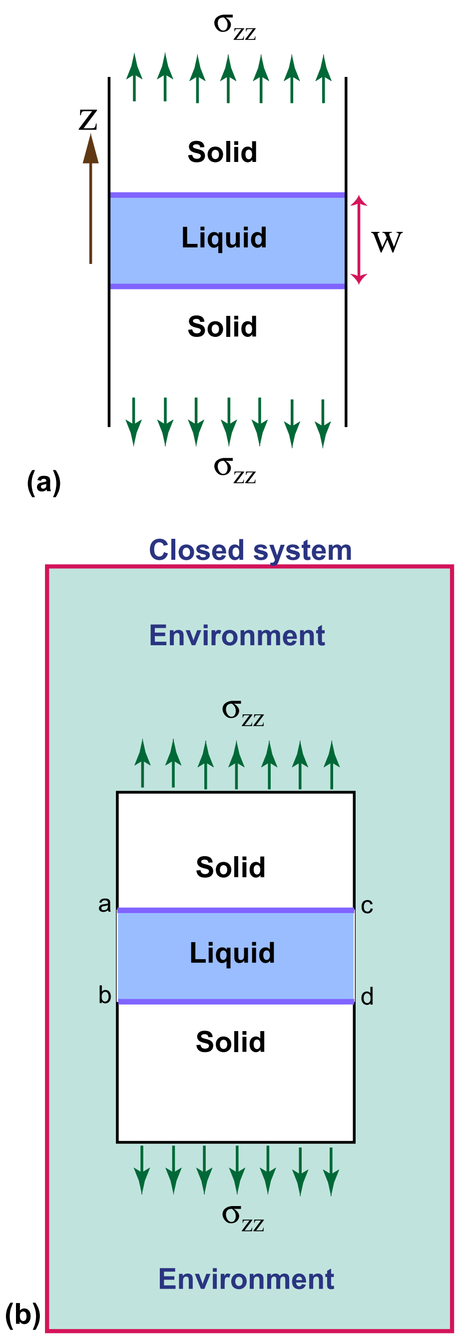

FIG. 1. Premelted GB subject to a normal stress σ_{zz}. (a) The GB region is modeled by a uniform liquid layer of width w bounded by interacting solid-liquid interfaces. (b) A thought experiment in which the GB is created in a closed system with rigid walls by the insertion of a liquid layer between two grains. The liquid layer can be thought of as growing by penetration of atoms from the environment through rigid but permeable side walls labeled *ab* and *cd*. The environment acts as a reservoir of energy and atoms kept a fixed temperature, pressure, and chemical potentials.

Note that each phase is specified by three independent variables (three degrees of freedom).

The equations of thermodynamic equilibrium between the phases are obtained from the condition $\delta F_L + \delta F_S = 0$ under the constraints of fixed volume and fixed number of atoms of each component. This gives

$$p_L^* = -\sigma_{zz}, \tag{3}$$

$$\Delta\mu^* = M^*, \tag{4}$$

$$\varphi_L(T,M^*,p_L^*) = \varphi_S(T,M^*,\sigma_{zz}). \tag{5}$$

Here and everywhere below, the asterisk marks properties related to thermodynamic equilibrium between the bulk phases. Equation (3) is the condition of mechanical equilibrium while Eqs. (4) and (5) are the conditions of chemical equilibrium and equilibrium with respect to the phase transformation, respectively. T and σ_{zz} play the role of control parameters. For each pair (T,σ_{zz}), Eqs. (3)–(5) can be solved for M^*, $\Delta\mu^*$, and p_L^*. Knowing these, $c_L^* = -(\partial\varphi_L/\partial\Delta\mu)_*$ and $c_S^* = -(\partial\varphi_S/\partial M)_*$ give the equilibrium chemical compositions of the phases. These compositions define two points on the solidus and liquidus lines of the equilibrium phase diagram.

Next, we consider a solid-liquid interface between the equilibrium phases. Following Gibbs' interface thermodynamics, we choose a geometric dividing surface inside the interface region. Suppose the precise position of this surface is adjusted so that the Gibbsian excess of the total number of atoms relative to this surface be zero: $\tilde{N} = 0$. We will use tilde to indicate excess quantities relative to this choice of the dividing surface. The solid-liquid interface free energy γ_{SL} is defined as the reversible work spent in forming a unit interface area. It can be presented in the form [48]

$$\gamma_{SL}A = \tilde{F} - M^*\tilde{N}_2, \tag{6}$$

where $\tilde{F}$ is the interface excess of free energy and $\tilde{N}_2$ is a similar excess of species 2.[2] Note that γ_{SL} is defined by Eq. (6) only in the state of phase equilibrium and is a function of two independent variables, e.g., T and σ_{zz}.

Now return to the liquid layer embedded between two grains [Fig. 1(a)]. Often, the layer is so thin that the inhomogeneous regions of the solid-liquid interfaces overlap. Thus the liquid layer is no longer homogeneous. However, in the model discussed here, the liquid is nevertheless treated as homogeneous and the solid-liquid interfaces are attributed the same properties as those of an equilibrium isolated interface at given T and σ_{zz}. The difference between this idealized picture and the real system is accounted for by introducing a coupling between the two interfaces called the disjoining interaction. The position of each interface is defined by the respective dividing surface for which $\tilde{N} = 0$. This choice of dividing surfaces ensures that, as the distance w between them increases, we eventually obtain two noninteracting interfaces

---

[2] In a more general treatment [48], γ_{SL} can be expressed in terms of generalized excesses introduced by Cahn. [49] For the purposes of this work it will suffice to use one particular type of excess, namely, $[X]_{NV}$, where X is any extensive property. To simplify the notations we denote this excess $\tilde{X}$. Equation (13) of Ref. [48] then reduces to $\gamma A = [U]_{NV} - T[S]_{NV} - M_{21}[N_2]_{NV}$, which in the present notations becomes Eq. (6).

discussed in the previous paragraph. In this limit, the liquid layer model becomes exact.

According to this model, the free energy of the system is

$$F = F_L(T,N_L,N_{2L},V_L) + F_S(T,N_S,N_{2S},V_S) + 2\tilde{F}(T,\sigma_{zz}) + \Psi(T,M,\sigma_{zz},w)A. \tag{7}$$

Here, F_L and F_S are the free energies of the phases computed assuming that they remain homogeneous all the way to the dividing surfaces, $\tilde{F}$ is the excess free energy of each solid-liquid interface, and Ψ is called the disjoining potential. Note that, due to our choice of the dividing surfaces, the total number of atoms in the system is $N = N_L + N_S$.

It is easy to derive the conditions of thermodynamic equilibrium in this system from the requirement that $\delta F = 0$ under the constraints of a closed system with a fixed volume: $\delta N_L + \delta N_S = 0$, $\delta N_{2L} + \delta N_{2S} = 0$, $\delta V_L + \delta V_S = 0$, and $\delta V_L = A\delta w$. Eliminating these constraints,

$$\delta F = (\varphi_L - \varphi_S)\delta N_L + (\Delta\mu - M)\delta N_{2L} + \left(\frac{\partial \Psi}{\partial w} - p_L - \sigma_{zz}\right)\delta V_L = 0$$

with three independent variations δN_L, δN_{2L}, and δV_L. The derivative

$$p_d = \frac{\partial \Psi}{\partial w} \tag{8}$$

is called the disjoining pressure. By definition, $\Psi \to 0$ and $p_d \to 0$ at $w \to \infty$. The equilibrium conditions become

$$p_d = p_L + \sigma_{zz}, \tag{9}$$

$$\Delta\mu = M, \tag{10}$$

$$\varphi_L(T,\Delta\mu,p_L) = \varphi_S(T,M,\sigma_{zz}). \tag{11}$$

Equation (9) shows that the liquid layer is subject to the disjoining pressure p_d in addition to the pressure $-\sigma_{zz}$ exerted by the solid. For each set of control parameters (T,M,σ_{zz}) defining the state of the solid, Eqs. (9)–(11) can be solved for the liquid properties $\Delta\mu$, p_L and p_d. The equilibrium width w is then the found from Eq. (8). The equilibrium compositions of the phases can be calculated from the relations $\partial\varphi_L/\partial\Delta\mu = -c_L$ and $\partial\varphi_S/\partial M = -c_S$.

B. Disjoining potential near the solidus line

If the liquid layer is thin, the phase compositions are different from the liquidus and solidus compositions at the same T and σ_{zz}. They only approach c_L^* and c_S^* if the liquid layer is thick enough to neglect the disjoining effect. Suppose T and σ_{zz} are fixed and M approaches M^*. The disjoining pressure is small and, to the leading order, is expected to be proportional to the undersaturation $\Delta M \equiv M - M^*$. Indeed, linearizing equation (11) with respect to the small parameters ΔM and p_d, we obtain

$$\varphi_L(T,M^*,-\sigma_{zz}) - c_L^*\Delta M + v_L^* p_d = \varphi_S(T,M^*,\sigma_{zz}) - c_S^*\Delta M.$$

The zeroth order terms cancel by Eq. (5) and we arrive at the equation relating the disjoining pressure to ΔM:

$$p_d = \frac{c_L^* - c_S^*}{v_L^*}\Delta M. \tag{12}$$

Similarly, for a single-component system close to the bulk melting point T_m, p_d is small and is expected to be proportional to the undercooling $\Delta T \equiv T - T_m$. In this case, the phase equilibrium conditions at and below T_m are, respectively,

$$\varphi_L(T_m,-\sigma_{zz}) = \varphi_S(T_m,\sigma_{zz}) \tag{13}$$

and

$$\varphi_L(T,p_d - \sigma_{zz}) = \varphi_S(T,\sigma_{zz}). \tag{14}$$

Linearizing Eq. (14) with respect to ΔT and p_d and using Eq. (13), we obtain

$$p_d = \frac{H_m}{v_L^* T_m}\Delta T, \tag{15}$$

where $H_m = (s_L^* - s_S^*)T_m$ is the heat of melting per atom, s_L^* and s_S^* being the entropies of the equilibrium phases per atom.

C. Fluctuations of grain boundary width

We now consider fluctuations within the liquid layer model of GB premelting. The starting point is the calculation of the GB free energy γ. The latter is defined as the reversible work spent on the creation of a unit GB area, or equivalently, the free energy change in a closed system incapable of performing work. The process of GB creation can be thought of as the insertion of a liquid layer of a given width w between the two grains [Fig. 1(b)]. During the insertion, the system draws the required amounts of atoms from an environment where the atoms are maintained at the temperature T, pressure p_L^0, and chemical potentials μ_1^0 and μ_2^0. Here, index 0 is a reminder that the relevant quantities are computed in the state of equilibrium described by Eqs. (9)–(11). It is assumed that the system and the environment form a closed system enclosed in a rigid envelop. Accordingly, the work $\hat{\gamma}A$ of forming a GB area A is

$$\hat{\gamma}A = F_L^0 + 2\tilde{F}(T,\sigma_{zz}) + \Psi(T,M^0,\sigma_{zz},w)A - \sigma_{zz}V_L - \mu_1^0 N_{1L} - \mu_2^0 N_{2L} - 2M^0\tilde{N}_2. \tag{16}$$

Here, F_L^0 is the free energy of the embedded liquid layer, the second and third terms account for the excess free energy of the two solid-liquid interfaces [cf. Eq. (7)], $\sigma_{zz}V_L$ is the work performed by the environment on the solid-liquid system, and the remaining terms give the free energy change of the environment due to the loss of atoms needed for the formation of the liquid layer and the interface segregation of component 2. Using the standard relation

$$\mu_1^0 N_{1L} + \mu_2^0 N_{2L} = F_L^0 + p_L^0 V_L,$$

Eq. (16) becomes

$$\hat{\gamma}A = F_L^0 + 2[\tilde{F}(T,\sigma_{zz}) - M^0\tilde{N}_2] + \Psi(T,M^0,\sigma_{zz},w)A - \left(\sigma_{zz} + p_L^0\right)V_L.$$

Applying Eqs. (6) and (9), we finally obtain

$$\hat{\gamma}(w) = 2\gamma_{SL} + \Psi(w) - p_d^0 w. \tag{17}$$

For brevity, we have suppressed T, M^0, and σ_{zz} as parameters of the disjoining potential and p_d^0.

It is important to recognize that $\hat{\gamma}(w)$ given by Eq. (17) is *not* the equilibrium GB free energy. While the solid and liquid phases satisfy the chemical and phase-change equilibrium conditions (10) and (11), the disjoining pressure is generally different from p_d^0 and the mechanical equilibrium condition (9) has not been satisfied. Note that w remains a free parameter, whose value affects the disjoining pressure through Eq. (8). This situation is an example of a quasiequilibrium state, in which subsystems of a thermodynamic system are in internal equilibria but not necessarily in full equilibrium with each other. As discussed in detail in a recent paper [46], the fundamental assumption of the thermodynamic fluctuation theory is that equilibrium fluctuations give rise to such quasiequilibrium states on the appropriate time scale.

The equilibrium GB free energy can be obtained by minimizing $\hat{\gamma}(w)$ with respect to w [recall that the right-hand side of Eq. (17) is the reversible work of GB formation and thus reaches a minimum at equilibrium]. If w_0 is the GB width at which $\hat{\gamma}(w)$ is a minimum, then the equilibrium GB free energy is

$$\gamma_0 = 2\gamma_{SL} + \Psi(w_0) - p_d^0 w_0. \tag{18}$$

The premelted GB fluctuates around its equilibrium state. To describe fluctuations of its width w, we consider only fluctuations of the disjoining interaction while treating all other thermodynamic parameters as properties of a large reservoir. The fluctuations bring the system to quasiequilibrium states mentioned above. Using the generalized canonical distribution (see, e.g., Eqs. (98) and (99) in Ref. [46]), the probability of finding w in an interval dw is

$$P(w)dw = P_m \exp\left[-A\frac{\Psi(w) - \Psi(w_0) - \left(\frac{\partial\Psi}{\partial w}\right)_0 (w - w_0)}{k_B T}\right]dw, \tag{19}$$

where k_B is Boltzmann's constant, P_m is the maximum value of the probability density $P(w)$, and $(\partial\Psi/\partial w)$ is the thermodynamic force conjugate to Ψ. According to this equation, w_0 is the most probable value of the GB width, i.e., the position of a peak of $P(w)$. Equation (19) can be rewritten in the form

$$P(w) = C \exp\left(-A\frac{\Psi(w) - p_d^0 w}{k_B T}\right), \tag{20}$$

where the pre-exponential coefficient C can be found from the normalization condition $\int_0^\infty P(w)dw = 1$. A similar equation was employed in previous studies of premelting in single-component systems [24,25,37]. Here, it has been extended to a binary system. Recall that for a binary system, p_d^0 is given by Eq. (12).

Equation (20) is the main equation used for the calculation of disjoining potentials from GB width fluctuations. It can be written in the alternative form [24,25,37]

$$P(w) = C' \exp\left(-\frac{\hat{\gamma}(w)A}{k_B T}\right), \tag{21}$$

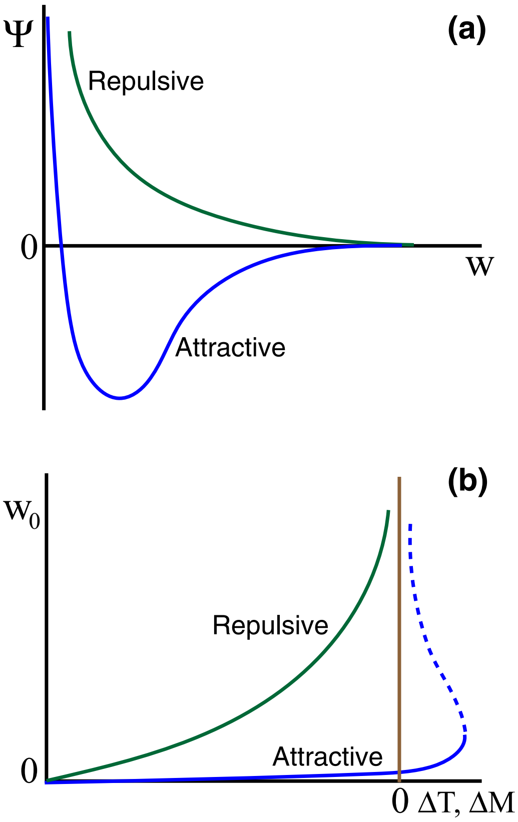

FIG. 2. Traditional classification of disjoining potentials into repulsive and attractive. (a) Potential shapes. (b) Equilibrium GB width as a function of undercooling ΔT or undersaturation ΔM for the two types of potentials. The vertical line marks the equilibrium melting point (respectively, solidus line). The dashed curve represents unstable GB states.

where C' is a normalization factor and $\hat{\gamma}(w)$ is the quasiequilibrium GB free energy given by Eq. (17).

We can also find the average GB free energy $\bar{\gamma}$ that incorporates the effect of width fluctuations. Averaging Eq. (17) over the width probability distribution (20), we obtain

$$\bar{\gamma} = 2\gamma_{SL} + \overline{\Psi(w)} - p_d^0 \bar{w}, \tag{22}$$

where the bar denotes averages[3]

$$\bar{w} = \int_0^\infty w P(w)dw, \tag{23}$$

$$\overline{\Psi(w)} = \int_0^\infty \Psi(w)P(w)dw. \tag{24}$$

D. Types of disjoining potentials

Two categories of disjoining potentials have been discussed in the literature: repulsive and attractive [24,25,29,33,36–38] [Fig. 2(a)]. For metallic systems, both the repulsive and

---

[3] Note the difference between the average values, such as $\bar{w}$ and $\bar{\gamma}$, and the previously introduced most probable values w_0, γ_0, etc. For highly asymmetric distributions, especially those with two local maxima, they can be significantly different.

attractive interactions are short-range and have a structural character: the attraction is due to the overlap of density perturbations near the solid-liquid interfaces and the repulsion arises from the orientation mismatch of the merging crystal lattices [24,25,33,36,37]. The repulsion and attraction are usually modeled by exponential functions. Both the repulsion and attraction can be described by a single functional form [33,38]

$$\Psi(w) = C_1 e^{-w/\delta_1} - C_2 e^{-w/\delta_2}, \qquad (25)$$

where the four coefficients C_1, C_2, δ_1, and δ_2 depend on the thermodynamic state of the grains. This functional form predicts two premelting scenarios: either continuous premelting with a logarithmic divergence of the GB width at the melting point (or solidus line), or a relatively narrow boundary that can be overheated above the melting point (respectively, oversaturated above the solidus line) until an instability point at which it abruptly melts [Fig. 2(b)].

A limitation of Eq. (25) is that it does not predict the thin-to-thick premelting transitions that were observed in phase field simulations [32,33] and the atomistic study described later in this paper. It was suggested [32] that such transitions require a nonexponential potential. Namely, that the potential shape have a concave region between two convex regions [Fig. 3(a)], so that a common tangent could be constructed with two different touching points. We call this type of a disjoining potential *intermediate*. The plot of $\hat{\gamma}$ versus w can then have two local minima giving rise to stable and metastable states of the boundary [Fig. 3(b)]. At an appropriate undercooling (undersaturation), the minima have an equal depth. This situation corresponds to equilibrium between two GB phases and is the point of a thin-to-thick transition [Fig. 3(c)]. Above this point, the GB width continues to increase and eventually diverges at the melting point (respectively, solidus line). In a binary system, such transitions can be represented by a thin/thick coexistence line below the solidus line on the equilibrium phase diagram. [32]

As the state of the grains varies, the disjoining potential can evolve from repulsive to intermediate to attractive. To describe this evolution, it is desirable to have a single analytical form of $\Psi(w)$ that describes all three cases, depending on the choice of the parameters. In this paper, we propose the following functional form:

$$\Psi(w) = c_1 e^{-c_2 w} - c_3 e^{-c_4 w} \sin(c_5 w + c_6), \qquad (26)$$

with six coefficients c_i. This form is a generalization of Eq. (25) and can be shown to capture all three cases. The first term describes exponential repulsion at small w. The sine in the second (attractive) term creates the intermediate shape mentioned above that leads to the thin-to-thick transition.

An additional effect captured by Eq. (26) is the presence of damped oscillations in the tail part of the disjoining potential. The incorporation of such oscillations is motivated by the existence of composition patterning near solid-liquid interfaces. Compositional oscillations in the liquid phase near solid-liquid interfaces were found in several alloy systems in both experiments [50–52] and simulations [48,53–55]. This effect was also found in the present work as illustrated in

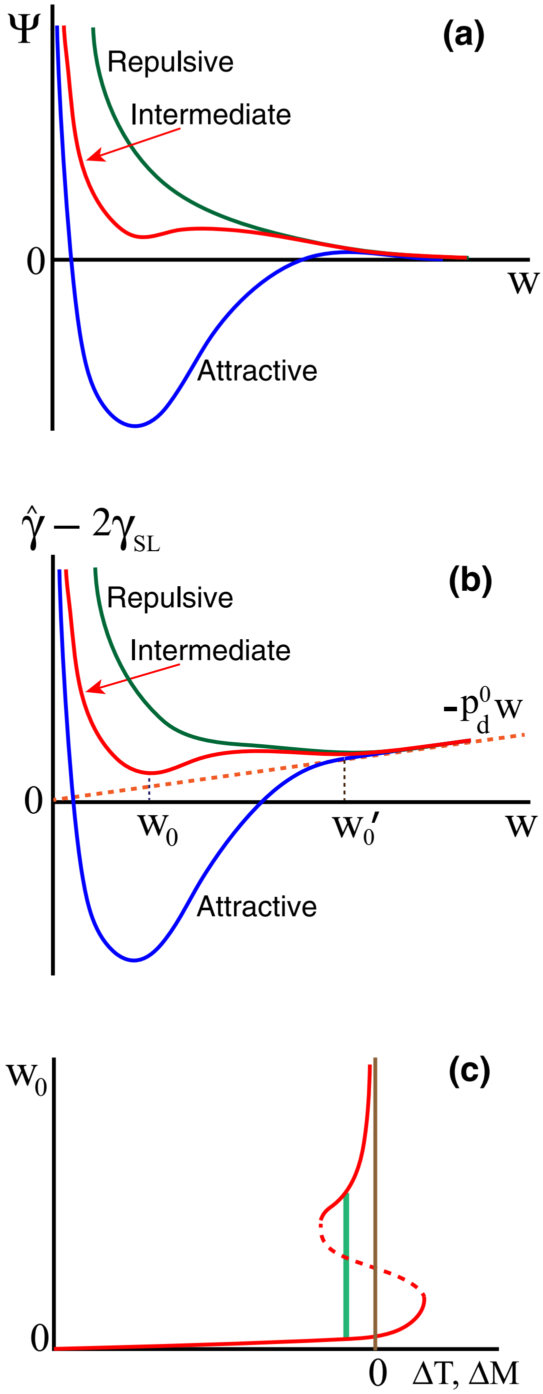

FIG. 3. Disjoining potentials proposed in this work: repulsive, attractive and intermediate. (a) Potential shapes. Note that the attractive and intermediate potentials have a shallow maximum in the tail region. (b) Nonequilibrium GB free energy $\hat{\gamma}$ relative to $2\gamma_{SL}$ as a function of GB width for the three potential types. The red dashed line represents the term $-p_d^0 w$. The minima of $\hat{\gamma}$ correspond to equilibrium GB states. Note that the intermediate potential creates two local minima corresponding to GB states with widths w_0 and w_0'. (c) Equilibrium GB width as a function of undercooling ΔT or undersaturation ΔM for the intermediate disjoining potential. The green vertical line shows the thin-to-thick transition in the GB. The long vertical line marks the equilibrium melting point (respectively, solidus line). The dashed curve represents unstable GB states.

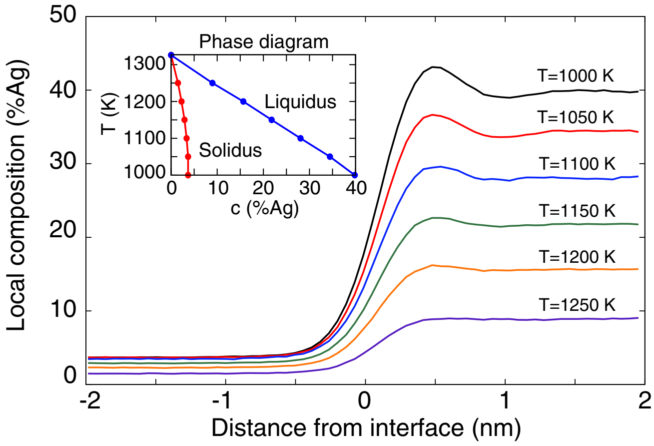

FIG. 4. Chemical composition profiles across the (210) solid-liquid interface in the Cu-Ag system at several temperatures. The interface position was determined from the order parameter profile as explained in the text. The inset shows the relevant portion of the phase diagram with the solid and liquid compositions marked by the points.

Fig. 4. The methodology of the simulations shown in this figure will be explained later. At this point, it is important to notice the compositional oscillations in the liquid near the solid-liquid interface. The peak of Ag concentration closest to the interface, which we call the principal peak, is followed by a set of local minima and maxima with fast decreasing amplitude until the composition levels out at c_L^*.

Similar compositional oscillations were found near the (110) oriented interface in the same system [48], pointing to the generality of the effect. In fact, simulations show that any static perturbation of chemical composition in this system produces a relaxation zone with oscillatory behavior of the chemical composition. For example, compositional oscillations were observed under an open surface of Cu-Ag melt [48]: underneath the topmost layer enriched in Ag relative to the bulk, there is a layer depleted in Ag, followed by a layer slightly enriched in Ag, and so on until the composition become practically uniform deeper in the bulk. In a premelted GB, the solid-liquid interfaces create a superposition of such compositional oscillations in a manner similar to wave interference. Since it is this overlap that gives rise to the disjoining attraction, we expect that the disjoining potential may display rapidly decaying oscillations in the tail region. The concave region mentioned above, and thus the thin-to-thick transition, are associated with the overlap of depletion zones. In principle, the higher-order peaks may create an entire cascade of additional thin-to-thick transitions closer to the solidus line. The situation is similar to the layering transitions [45] in surface adsorption and would give rise to a set of tightly spaced transition lines on the phase diagram, each ending at a critical point.

III. METHODOLOGY OF SIMULATIONS

A. Simulation of bulk phases

Atomic interactions in the Cu-Ag system were described by the embedded-atom method (EAM) [56] potential [57] that accurately predicts a large number of properties of Cu and Ag and was fitted to a first-principles database of Cu-Ag compounds. The potential reproduces the Cu-Ag phase diagram in reasonable agreement with experiment (Fig. 5).

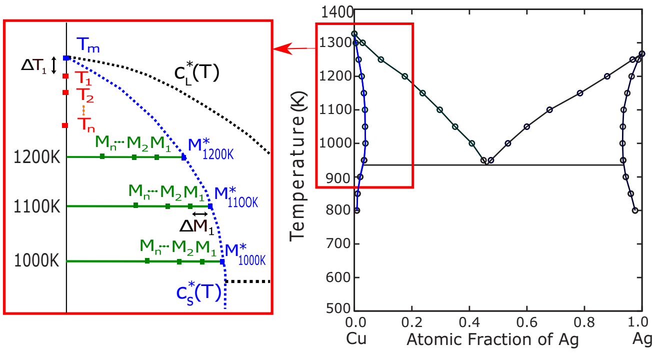

FIG. 5. (Right) Phase diagram of the Cu-Ag system calculated with the EAM potential [57] utilized in this work. (Left) Zoomed-in view of the Cu rich side of the phase diagram showing the sampling method of temperatures and compositions studied in this work.

Although MD was the main simulation method used in the previous GB premelting studies in pure metals [24,25], this method is not well suited for alloy systems. As mentioned above, the accessible MD simulation times are too short to achieve chemical equilibrium of the premelted GB structure by atomic diffusion through the solid solution. Hence MC simulations were chosen as the main simulation method, as was done in the previous work [57]. For consistency of methodology, MC was also used in premelting simulations of pure Cu, even though MD could have been applied. We utilized the parallel MC code developed by V. Yamakov at NASA [58,59]. Two MC modes were implemented in this work: the semigrand canonical ensemble and the composition-controlled algorithm.

In semigrand canonical MC simulations [60,61], the temperature T and the diffusion potentials M of Ag relative to Cu are fixed while the chemical composition is allowed to vary. In this work, the chemical composition was measured as a fraction of Ag atoms. Depending on the goal of the simulation, some or all of the system dimensions were allowed to vary. The trial moves of the MC process included displacements of randomly selected atoms by a small random amount in a random direction with simultaneous random reassignment of the chemical species of the chosen atom to either Cu or Ag. The number of trial moves equal to the number of atoms in the system constitutes one MC step. After each MC step, the dimensions of the simulation block in all or some of the x, y, and z directions were altered by random amounts with appropriate rescaling of atomic coordinates. Such fluctuations of the system dimensions ensure zero normal stresses σ_{ii} in the respective directions ($i = x,y,z$). The trial moves were accepted or rejected by the Metropolis algorithm [60,61]. Namely a move was accepted with the probability $\exp(-\Omega/k_B T)$ if $\Omega > 0$ and unconditionally if $\Omega \leqslant 0$, where [62–64]

$$\Omega \equiv \Delta E \pm M \pm \frac{3}{2} k_B T \ln \frac{m_{\mathrm{Cu}}}{m_{\mathrm{Ag}}}. \tag{27}$$

Here, m_{Cu} and m_{Ag} are atomic masses of Cu and Ag and ΔE is the energy change due to the trial move. The positive sign applies when Cu is replaced by Ag and negative when Ag is replaced by Cu. The logarithmic term with atomic masses comes from the integration of the state probability over the linear momenta of atoms, giving a preexponential factor proportional to the product of masses of all atoms to the power of $3/2$. In the probability ratio of two atomic configurations, all masses cancel out except for the masses of the atom whose species changes, giving rise to the pre-exponential factor of either $(m_{\mathrm{Cu}}/m_{\mathrm{Ag}})^{3/2}$ or $(m_{\mathrm{Ag}}/m_{\mathrm{Cu}})^{3/2}$. The MC simulations bring the system to thermodynamic equilibrium under the imposed boundary conditions. Since the redistribution of chemical species is implemented by an artificial procedure that does not require diffusion, chemical equilibrium is achieved much faster than in MD. Once equilibrium is reached, a long MC run was implemented to compute expectation values of thermodynamic properties in the given statistical ensemble. In the case of pure Cu, the canonical ensemble was implemented, which included all of the foregoing steps except that the chemical species of the atoms remained unaltered.

The composition-controlled MC simulations [58,59,64] impose a desired average chemical composition c of the simulation block and let the system adjust the diffusion potential M to achieve this composition. To reach the preset composition c, a feedback loop is created between the current value of c and the imposed diffusion potential M according to the iteration scheme

$$M^{(n)} = M^{(n-1)} - a\left(\frac{c^{(n-1)} + c^{(n-2)}}{2} - c\right), \qquad (28)$$

where index n labels MC steps and a is an adjustable parameter that controls the computational efficiency of the simulation without affecting the result. After the system reaches equilibrium, both the composition and diffusion potential slightly fluctuate around their equilibrium values. It can be shown [64] that the feedback algorithm is similar to the variance constrained MC method proposed by Sadigh *et al.* [65]

The study of GB premelting required the knowledge of thermodynamic properties of the bulk solid and liquid phases and the exact positions of the solidus and liquidus lines on the phase diagram. To compute thermodynamic properties of the solid solution, we used a cubic simulation block containing 5324 perfect lattice cites with periodic boundary conditions. Stress-free ($\sigma_{xx} = \sigma_{yy} = \sigma_{zz} = 0$)[4] semigrand canonical MC simulations were executed for a set of temperature-composition pairs (T,c) with the desired compositions achieved by properly choosing the diffusion potential. Typically, the system was equilibrated by 3×10^4 MC steps followed by 2×10^5 production steps to gather statistics. The pairs (T,c) were chosen to sample the regions of interest on the phase diagram for both GB premelting simulations and thermodynamic integration as will be discussed later. For each (T,c), a set of properties was computed including the diffusion potential, the average potential energy per atom, and the thermochemical expansion factor of the lattice relative to pure Cu at 0 K. Similar calculations were conducted for pure Cu ($c = 0$) for a chosen set of temperatures.

TABLE I. Solid-liquid coexistence properties on the Cu-rich side of the Cu-Ag system; the diffusion potential M^*, the solidus and liquidus compositions c_S^* and c_L^*, and the volume per atom in the liquid phase v_L^*. 1325.25 K is the estimated melting point of pure Cu.

T (K)	M^* ($\frac{\mathrm{eV}}{\mathrm{atom}}$)	c_L^* (%Ag)	c_S^* (%Ag)	v_L^* ($\frac{\mathrm{nm}^3}{\mathrm{atom}}$)
1000	0.5692	39.83	3.69	.01552
1100	0.5194	28.06	3.36	.01493
1200	0.4437	15.66	2.26	.01426
1325.25	–	0	0	.01339

Although the approximate positions of the solidus and liquidus lines predicted by this interatomic potential were known from previous calculations [57] (Fig. 5), the premelting simulations required a more precise knowledge of the solidus and liquidus compositions, c_S^* and c_L^*, at temperatures of interest. They were calculated at the temperatures of 1000, 1100, and 1200 K by the following phase-coexistence procedure. A rectangular periodic simulation block was prepared with dimensions of approximately $4 \times 4 \times 16$ nm containing 22 000 atoms. The block contained two regions filled with the solid and liquid phases separated by a (210)-oriented solid-liquid interface normal to the long direction z. The lattice of the solid phase was pre-expanded according to the equilibrium lattice parameter at the chosen temperature and the equilibrium diffusion potential M^* estimated in the previous work [57]. Since the final values of M^* were close to the initial estimates, the solid phase remained virtually stress-free. Next, a composition-controlled MC simulation run was executed at a fixed cross-section of the simulation block and zero-stress condition imposed in the z direction. Knowing the previously estimated c_S^* and c_L^* values, the imposed chemical composition c was selected by the lever rule so as to give an approximately 50:50 volume fraction of both phases. After equilibration, a 3×10^6 MC step simulation was performed to compute refined values of M^*, c_S^*, and c_L^*. The latter were obtained by averaging the compositions of bulk regions inside each phase unaffected by the interface. The results are summarized in Table I, which also includes the computed atomic volume v_L^* of the liquid phase.

Similar calculations were performed for solid-liquid coexistence in pure Cu, excepts that the MC ensemble was canonical. While our previous calculations [57] and work by other authors suggested that the melting temperature predicted by the present EAM potential is between 1326 and 1327 K, in this work we find that $T_m = 1325.25$ K provides more consistent results for GB premelting (see details below). The 1-K scatter of the temperatures may reflect system size effects and/or limitations of different calculation methods. At 1325.25 K, there was no discernible growth of either phase during the longest MC simulation runs that we could afford. The melting enthalpy H_m was calculated from the energy difference between the phases at 1325.25 K. The obtained $H_m = 0.1239$ eV/atom is in good agreement with 0.1244 eV/atom reported previously [57].

---

[4] Although in the model of Sec. II, the solid was subject to a nonzero stress to keep the analysis more general, the simulations conducted in this work implemented a particular case when the grains remain stress-free.

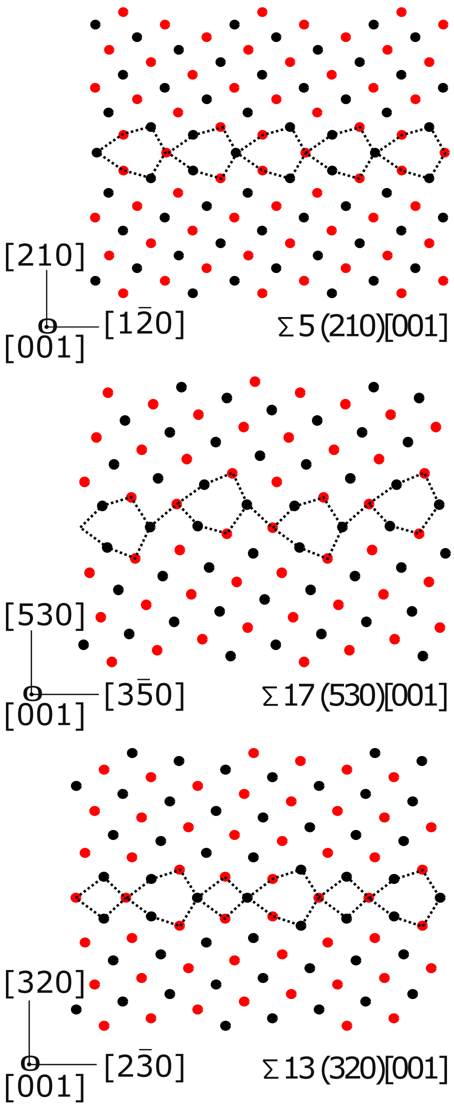

FIG. 6. Atomic structures of three GBs studied in this work. The tilt axis [001] is normal to the page and the kite-shaped structural units are outlined. The red and black atoms belong to alternating (002) atomic planes.

B. Grain boundary simulations

Three symmetric tilt GBs were studied in this work: Σ5(210)[001], Σ17(530)[001], and Σ13(320)[001]. Here, Σ is the reciprocal density of coincident sites, [001] is the tilt axis, and the symbols in parentheses indicate the GB plane. In the remainder of the paper, these boundaries will be refereed to as Σ5, Σ17, and Σ13, respectively. Their 0 K structures were obtained by applying standard geometric constructions and minimizing the total energy with respect to local atomic displacements and rigid translations of the grains relative to each other [66]. The GB structures obtained are in agreement with previous simulations [67] as shown in Fig. 6. Their 0 K energies, misorientation angles and dimensions of the periodic simulation blocks are listed in Table II. Note that the GB energy decreases in the order Σ5, Σ17, and Σ13.

For pure Cu GBs, canonical MC simulations were performed at several temperatures from 100 K to 1324 K (1 K below the melting point). As with bulk simulations, the system was preexpanded by the known thermal expansion factor of the lattice. The (x,y) cross-section of the simulation block was then fixed while the z dimension (normal to the GB plane) was allowed to fluctuate to maintain the $\sigma_{zz}=0$ condition. These boundary conditions ensured zero stress inside the grains while allowing the thermal expansion of the GB region to be different from that of the lattice.

TABLE II. Properties of the three symmetrical tilt GBs studied in this work; the lattice rotation angle around the [001] tilt axis, the 0-K GB energy γ, the number of atoms in the simulation block N, and the block dimensions. The GB plane is normal to the z axis.

Boundary	Tilt angle	γ (J/m^2)	N	L_x (nm)	L_y(nm)	L_z(nm)
Σ5(210)	53.13°	0.951061	22000	4.04	3.98	16.17
Σ17(530)	61.93°	0.856302	21216	4.23	4.69	12.63
Σ13(320)	67.38°	0.790050	29120	5.21	5.06	13.03

At temperatures below 1280 K, the GB structures were relatively ordered and premelting was not a consideration. Simulations at these temperature were carried out solely to obtain data needed for the subsequent thermodynamic integration (see Secs. III E and IV A 2). At each temperature, the system was equilibrated by 10^5 MC steps before a production run for 5×10^5 MC steps. Snapshots were saved every 2000 steps. Above 1280 K, the simulations were run much longer (typically, between 4×10^6 and 3×10^7 MC steps) in order to obtain sufficient statistics of GB width fluctuations. The temperature step was reduced as temperature increased. The temperatures closest to the melting point were 1300, 1310, 1315, 1320, and 1324 K.

For binary alloys, the simulation block was similarly pre-expanded according to the lattice parameter at the chosen temperature and grain composition. Semigrand canonical MC simulations were carried out with a fixed GB cross-section and fluctuating z dimension maintaining the $\sigma_{zz}=0$ condition. At each of the three temperatures studied (1000, 1100, and 1200 K), the simulations were run for two sets of diffusion potentials. The first set started with dilute alloys and sampled grain composition far away from the solidus line. Such simulations were only needed for thermodynamic integration as will be discussed later. The second set included grain compositions very close to the solidus line and was designed for the fluctuation analysis of the GB width. The numbers of MC steps implemented in both sets were similar to those for pure Cu far away and close to the melting point, respectively.

To verify that the scaling of the lattice indeed ensured zero-stress conditions inside the grains, multiple snapshots containing local stress data were averaged to compute the stress profiles $\sigma_{ij}(z)$. For both pure Cu and Cu-Ag alloys, such profiles showed a nearly perfect zero stress inside the grains and a sharp spike of σ_{xx} and σ_{yy} caused by the interface stress in the GB regions.

C. Calculation of the grain boundary width distribution

The width w of a premelted GB was identified with the width of the liquid layer formed inside the boundary. The first step in calculating w was to construct an order parameter

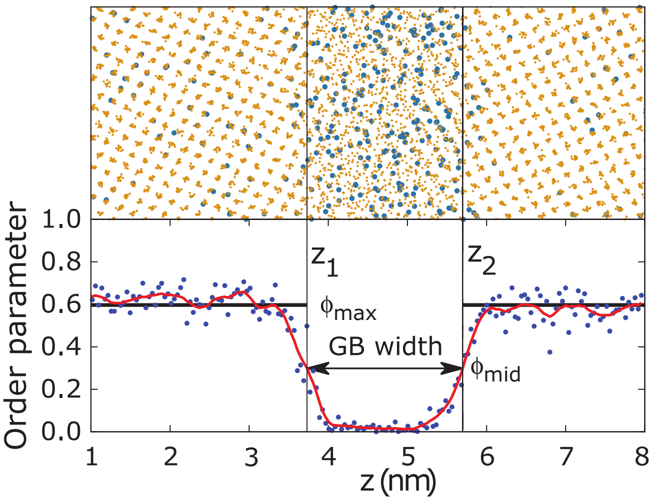

FIG. 7. Typical order parameter profile used to calculate the GB width in a single snapshot. The blue points are raw values of the structure factor $|S_i|(z_i)$ and the red curve is the smoothed profile $\phi_i(z_i)$. The simulation was for the $\Sigma 5$ GB at 1200 K with the grain composition of 2.23 at.%Ag. The upper image shows the atomic positions projected along the [001] tilt axis normal to the page, with yellow points representing Cu atoms and blue points Ag atoms.

profile across the boundary. As such, we chose the parameter characterizing the periodic order of the (002) crystal planes normal to the tilt axis [001] (y direction) [23,48,68]. This order parameter is the modulus of the structure factor $S(\boldsymbol{k})$ computed for a set of bins parallel to the GB plane:

$$|S_i(\boldsymbol{k})| = \sqrt{\left(\frac{\sum_j \cos(\boldsymbol{k}\cdot\mathbf{r}_j)}{N_i}\right)^2 + \left(\frac{\sum_j \sin(\boldsymbol{k}\cdot\mathbf{r}_j)}{N_i}\right)^2}, \tag{29}$$

where $\boldsymbol{k} = 2\pi(0,2/a,0)$ is the reciprocal lattice vector, $\mathbf{r}_j$ is the position of atom j in bin i, a is the cubic lattice parameter in the grains, and the summation runs over all N_i atoms in the bin. This order parameter is unity in the perfect crystal at 0 K, has a positive value smaller than 1 in the grains at finite temperatures, and is zero in the liquid phase. An example of an order parameter profile $|S_i|(z_i)$ computed from a single snapshot is shown in Fig. 7, z_i being the center of bin i and the bin width was 0.0615 nm. The scatter of the points is due to thermal noise. To mitigate the noise effect, a smoothing procedure was applied where each of the $|S_i|$ values was averaged with two neighboring points on either side. This resulted in a smoothed profile that we denote $\phi_i(z_i)$ and show as a red curve in Fig. 7 (the discrete points are connected by line segments).

The grain value ϕ_{max} was computed by averaging over regions far away from the GB. Next, two locations z_1 and z_2 were found at which the order parameter was equal to $\phi_{\mathrm{mid}} = \phi_{\mathrm{max}}/2$. Because the function $\phi_i(z_i)$ is discrete, linear interpolation of ϕ_i was applied to find z_1 and z_2. The GB width was then defined as the difference $w = |z_1 - z_2|$. Note that, due to the periodic boundary conditions, each snapshot effectively contained two GBs, both of which were used to calculate w. For the alloy system, the chemical composition profile could be alternatively used to calculate w. However, we chose to use the structural order parameter throughout this work to ensure consistency between the alloy and pure Cu simulations.[5]

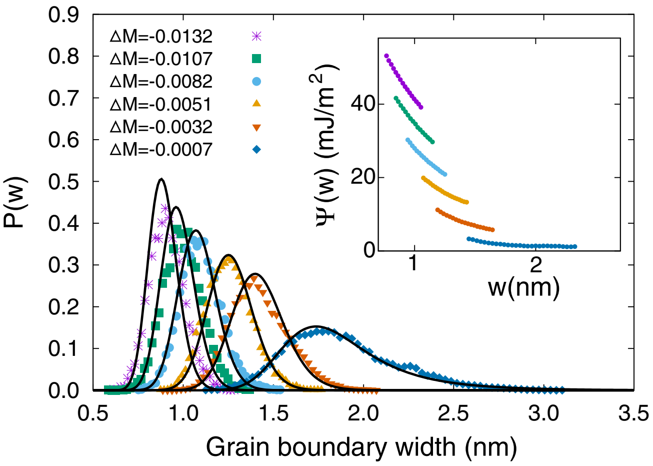

FIG. 8. Probability density functions $P_i(w_i)$ for different values of ΔM (in eV) computed for the $\Sigma 5$ GB at the temperature of 1000 K. The inset shows the segments of the disjoining potential extracted from these functions. The curves are the normalized distributions predicted by the analytical disjoining potential.

The described calculation of w was repeated for all N_p snapshots saved in each simulation. The number of snapshots increased as the simulation condition approached the solidus line. From the entire set of GB widths obtained in a simulation, a histogram was constructed using the number of bins $2(N_p)^{1/3}$ (the Rice rule). The histogram was then scaled by the bin width and divided by N_p to obtain a discrete probability density function $P_i(w_i)$ normalized to unity of its midpoint Riemann sum. As an example, Fig. 8 shows a set of probability functions for the $\Sigma 5$ boundary at 1000 K. In total, twelve such sets were generated in this work (three GBs, three temperatures for the alloys, and one temperature set for pure Cu).

D. Calculation of the disjoining potential

As discussed in Sec. II C, the GB width distribution $P(w)$ is related to the disjoining potential $\Psi(w)$ by Eq. (20). Inverting this equation, we get

$$\Psi(w) = -\frac{k_B T}{A}\ln P(w) + p_d^0 w + D, \tag{30}$$

where D is the logarithm of the normalization coefficient. Recall that p_d^0 is given by Eq. (15) for pure Cu and by Eq. (12) for a Cu-Ag alloy, the superscript 0 being a reminder that this disjoining pressure is computed at the bulk solid-liquid equilibrium. The undercooling temperature

---

[5] As indicated in Sec. II A, the GB width w is defined as the distance between two dividing surfaces in the solid-liquid interfaces satisfying the condition $\tilde{N} = 0$. The described practical definition of w through the order parameter profile need not satisfy this condition and constitutes an approximation. The larger w, the more accurate this approximation becomes.

ΔT and undersaturation potential ΔM are known in each simulation.

Ideally, if the function $P(w)$ could be computed accurately over the entire range $0 \leqslant w < \infty$, the coefficient D could be determined from the normalization condition $\int_0^\infty P(w)dw = 1$. The entire disjoining potential $\Psi(w)$ could be then obtained from a single simulation. In reality, a reliable calculation of $P(w)$ is limited to a certain interval around the peak and accurate normalization is unfeasible. Since D remains unknown, a single simulation recovers only a segment of $\Psi(w)$ up to an arbitrary vertical shift D. Examples of such segments are shown in Fig. 8. In this work, each segment was obtained from the probability distribution function in the interval $\bar{w} \pm 1.5\sigma$, where $\bar{w}$ is the average GB width estimated from the given distribution and σ is the standard deviation of the distribution.[6] The points outside this interval had relatively small probabilities and were usually not fully converged. Accordingly, they were not included in the calculation. Note that the segments calculated at different undercoolings (respectively, undersaturations) were defined in overlapping width intervals.

The next step was to join the segments together into a single continuous curve. This was accomplished by shifting the segments relative to each other so as to minimize the mean-square deviation between neighboring segments in the overlap intervals. Since the segments did not generally share the same mesh, they had to be remapped onto a common mesh in the overlap region using a linear interpolation scheme. The minimization was then implemented on this common mesh. Once the shifts were optimized, the values of $\Psi(w)$ in the overlap regions were obtained by averaging over the two segments on the common mesh.

This procedure resulted in a continuous curve defined up to a rigid shift that remained an unknown parameter. The postulated analytical potential given by Eq. (26) was then fitted to this curve. To this end, the mean-square deviation between the curve and the function was minimized with respect to six fitting parameters c_i plus the rigid shift.[7]

E. Calculation of properties for thermodynamic integration

Calculations of the GB free energy by thermodynamic integration required the knowledge of certain GB and bulk properties as functions of temperature and/or grain composition. Such properties include $\tilde{U}$, $\tilde{N}_2$, L_x, L_y, τ_{ii}, $(\partial e_{ii}/\partial T)_{c=0}$, $(\partial e_{ii}/\partial c)_T$ $(i = 1,2)$, and $(\partial M/\partial c)_T$. Here, c is the grain composition (it was earlier denoted c_S in the context of solid-liquid coexistence; we can now simplify the notation).

For GBs, the tilde sign denotes the Gibbsian excesses computed at a fixed number of atoms ($\tilde{N} = 0$).[8] In pure Cu, the excess energy $\tilde{U}$ was first computed in each snapshot by the following procedure. Knowing the locations of the two GBs from the order parameter profile, a layer containing each boundary together with surrounding grain regions was selected. Let the total energy and total number of atoms in both layers together be U_I and N_I, respectively. The rest of the simulation block was comprised of lattice regions unperturbed by the GBs. Their total energy U_g and number of atoms N_g represented a reference grain system. The excess $\tilde{U}$ was computed from the equation

$$2\tilde{U} = U_I - N_I\frac{U_g}{N_g}, \tag{31}$$

where the factor of 2 takes into account that the right-hand side represents two GBs. This $\tilde{U}$ was then averaged over all snapshots saved during the simulation. In alloys simulations, the excess Ag amount was computed in a similar manner using the equation

$$2\tilde{N}_2 = N_{2I} - N_I\frac{N_{2g}}{N_g}. \tag{32}$$

The cross-sectional dimensions of the GB, L_x and L_y, were known as functions of temperature and grain composition from the perfect-lattice simulations described in Sec. III A. From these data, the derivatives

$$\left(\frac{\partial e_{11}}{\partial T}\right)_{c=0} = \frac{1}{L_x}\left(\frac{\partial L_x}{\partial T}\right)_{c=0},$$

$$\left(\frac{\partial e_{22}}{\partial T}\right)_{c=0} = \frac{1}{L_y}\left(\frac{\partial L_y}{\partial T}\right)_{c=0}, \tag{33}$$

$$\left(\frac{\partial e_{11}}{\partial c}\right)_T = \frac{1}{L_x}\left(\frac{\partial L_x}{\partial c}\right)_T,$$

$$\left(\frac{\partial e_{22}}{\partial c}\right)_T = \frac{1}{L_y}\left(\frac{\partial L_y}{\partial c}\right)_T \tag{34}$$

were calculated by numerical differentiation using polynomial fits through the relevant sets of temperatures or compositions. The GB area $A = L_xL_y$ was also calculated as a function of temperature and/or composition.

The diffusion potentials and the respective grain compositions were known from the MC simulations of bulk

---

[6] For bimodal distributions, the segment of $\Psi(w)$ was calculated in the interval $0.8 \leqslant w \leqslant 2.2$ nm that encompassed both peaks. The rest of the distribution consisted of very small probabilities and was excluded.

[7] Formally, extrapolation of $\Psi(w)$ to $w \to 0$ gives $(\gamma_{\text{dry}} - 2\gamma_{SL})$, where γ_{dry} is the free energy of a hypothetical "dry" GB in which the two solid-liquid interfaces are infinitely close to each other. Clearly, in this limit the entire liquid layer model loses its physical meaning. On the other hand, since the simulations only sampled GB widths larger than several Angstroms, the function fitted in this width interval could display totally unreasonable behavior when extrapolated to the $w \to 0$ limit. Therefore we chose to impose the boundary condition $\Psi(w) \to (\gamma_{\text{dry}} - 2\gamma_{SL})$ at $w \to 0$ with a small weight during the curve fitting. We approximated γ_{dry} by the GB energy at 0 K and used the γ_{SL} values obtained by forcing the liquid layer model to match the thermodynamic integration result at the last point of the simulations (see text for more detail). This condition did not practically affect the quality of the fit in the physically meaningful width interval but gave a reasonable order of magnitude of $\Psi(w)$ at $w \to 0$.

[8] In terms of generalized excesses describing GBs [69,70], $\tilde{X}$ is equivalent to $[X]_N$, X being any extensive property. In Sec. II, we used the tilde symbol to denote Gibbsian excesses relative to a solid-liquid interface. From now on, this symbol denotes the excesses $[X]_N$ related to the entire GB region.

phases discussed in Sec. III A. The derivative $(\partial M/\partial c)_T$ was computed from a polynomial fit through the set of points (M,c) at a fixed temperature.

The interface stress was calculated from the relation [48,70–73]

$$\tau_{ii} = \frac{\sigma_{ii} V}{A}, \quad i = 1,2, \tag{35}$$

V being the system volume. This equation assumes zero stress outside the GB region, which was ensured in the present simulations. The work term $\sigma_{ii} V$ was computed by summing up the virial stress tensors over all atoms inside the interface layer (containing the GB and grain regions) and averaging over all snapshots.

Finally, thermodynamic integration required the knowledge of one reference value γ_{ref} of the GB free energy. To obtain it, the free energy of each GB in pure Cu was calculated in the quasiharmonic approximation at the reference temperature $T_{\text{ref}} = 300$ K as in previous work [70,71,74]. The values obtained were 0.888, 0.798, and 0.737J/m^2 for the $\Sigma 5$, $\Sigma 17$, and $\Sigma 13$ GBs, respectively.

It should be emphasized that the excess quantities discussed here are not parameters of the liquid layer model of GB premelting and were only generated in this work to provide input to the thermodynamic integration procedure for computing the GB free energy γ. These independently calculated values of γ will be tested against prediction of the liquid layer model in Sec. IV B 3.

IV. SIMULATION RESULTS AND INTERPRETATION

A. Grain boundary premelting in pure Cu

1. Premelting behavior and disjoining potentials

In all three GBs studied, the formation of a liquid layer was observed as the bulk melting point was approached from below; however, the extent of premelting was different. Figure 9 illustrates the gradual accumulation of disorder in the $\Sigma 5$ GB with increasing temperature culminating in the formation of a thick liquid layer a few degrees below T_m. To demonstrate the differences between the GBs, Fig. 10 shows typical snapshots at $\Delta T = -15.25$ K together with the width probability distributions. While the $\Sigma 5$ and $\Sigma 17$ GBs are strongly premelted at this temperature, the $\Sigma 13$ GB is disordered but not to the extent that it could be described as a liquid layer. These different behaviors are reflected in different positions of the peak of the GB width distribution.

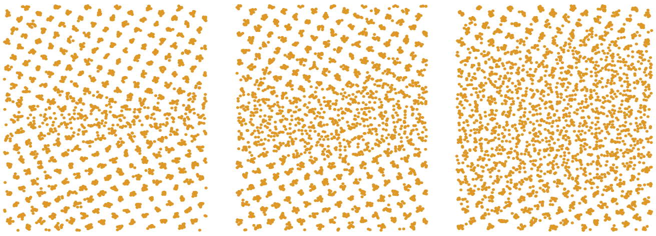
T=1100 K (-225.25 K) T=1300 K (-25.25 K) T=1324 K (-1.25 K)

FIG. 9. Premelting of the Cu $\Sigma 5$ GB at three different temperatures below the bulk melting point. The atomic positions are projected along the [001] tilt axis normal to the page. The number in parentheses is the undercooling ΔT.

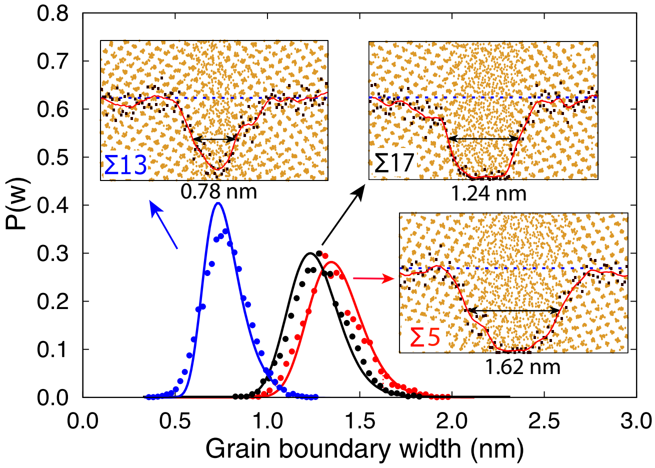

FIG. 10. Width probability distributions $P(w)$ for three GBs in Cu at 1310 K ($\Delta T = -15.25$ K) with snapshots of the premelted structures. The points represent the original histograms while the curves are the normalized distributions predicted by the analytical disjoining potential. The atomic positions are projected along the [001] tilt axis normal to the page. The numbers indicate the GB widths in the snapshots.

The plots of the average (over the probability distribution) GB width $\bar{w}$ as a function of undercooling ΔT (Fig. 11) indicate that, in all three GBs, the liquid layer thickness diverges to infinity at the bulk melting point. As discussed in Sec. II, this behavior is indicative of a repulsive disjoining potential.

As mentioned above, the disjoining potentials reconstructed from individual segments (Fig. 12) were initially defined up to an unknown rigid shift. They were then fitted by the analytical function in Eq. (26) with six parameters plus the rigid shift as the seventh fitting parameter. Figure 13 summarizes the disjoining potentials for the three GBs with optimized rigid shifts. By its physical meaning, $\Psi(w)$ must approach zero in the limit of $w \to \infty$ (no interaction between

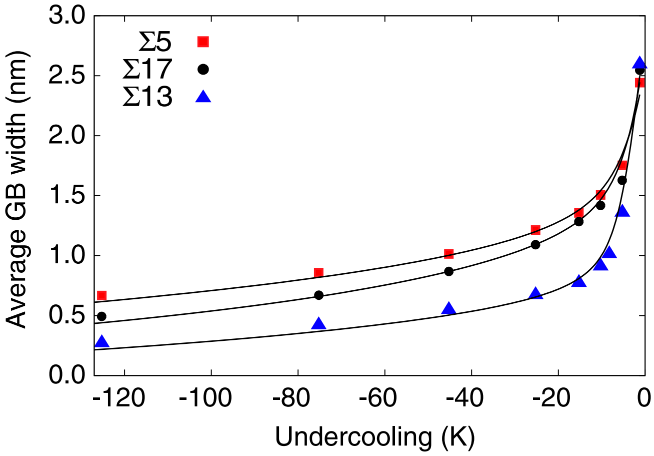

FIG. 11. Average GB width $\bar{w}$ as a function of undercooling ΔT for the pure Cu GBs.

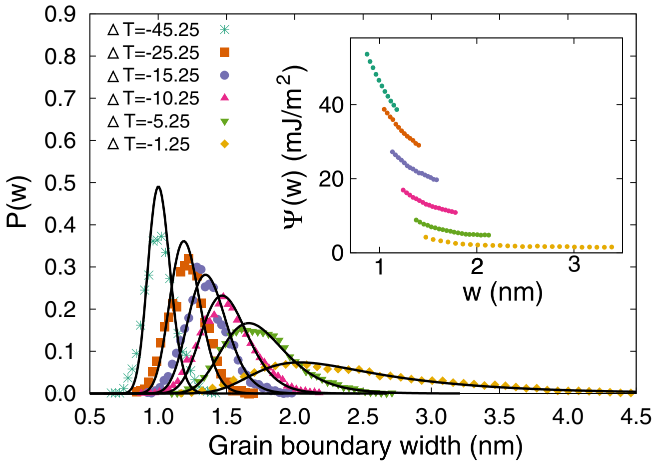

FIG. 12. Probability density functions for different undercoolings ΔT (in K) for the $\Sigma 5$ GB in pure Cu. The points represent the original histograms while the curves are the normalized distributions predicted by the analytical disjoining potential. The inset shows segments of the disjoining potential obtained by inversion of individual probability functions.

isolated solid-liquid interfaces). Note, however, that at the largest GB widths sampled in the simulations, some of the obtained $\Psi(w)$ points are slightly above or slightly below zero due to statistical errors. Such deviations from zero are especially pronounced for the $\Sigma 13$ GB at $w > 3.5$ nm. For this boundary, the deviations could represent a combined effect of statistical errors and systematic factors. Indeed, the $\Sigma 13$ boundary remains rather narrow and displays only slight premelting until a few degrees below the melting point. Under such conditions, modeling this boundary by a liquid layer is a more drastic approximation than for the $\Sigma 5$ and $\Sigma 17$ GBs.

As evident from Figs. 10–13, the $\Sigma 5$ GB exhibits the most extensive premelting and can be represented by a liquid layer most accurately. Accordingly, we expect that its disjoining potential must be exponentially repulsive and become practically zero at $w > 3.5$ nm. It was found that to meet this condition, a precise adjustment of the bulk melting point of Cu was necessary. As already mentioned, $T_m = 1325.25$ K was found to give the most accurate agreement with zero Ψ at $w > 3.5$ nm. With this melting temperature, the disjoining potential of the $\Sigma 5$ GB could be fitted by a purely exponential function [$c_3 = 0$ in Eq. (26)]. By contrast, accurate fitting for the $\Sigma 17$ and $\Sigma 13$ GBs required all terms in Eq. (26). Note that for the $\Sigma 13$ GB, the disjoining potential below 1.5 nm exhibits a characteristic shape suggestive of a developing shoulder.

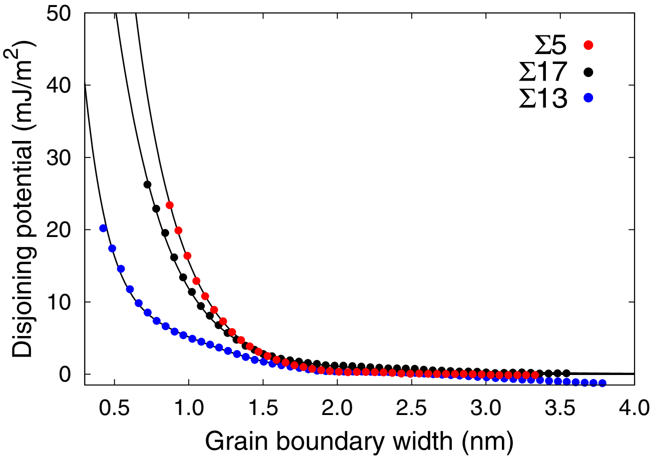

FIG. 13. Disjoining potentials for three GBs in pure Cu. The points represent simulation results from the GB width fluctuations. The solid lines are analytical disjoining potentials fitted to the points as discussed in the text.

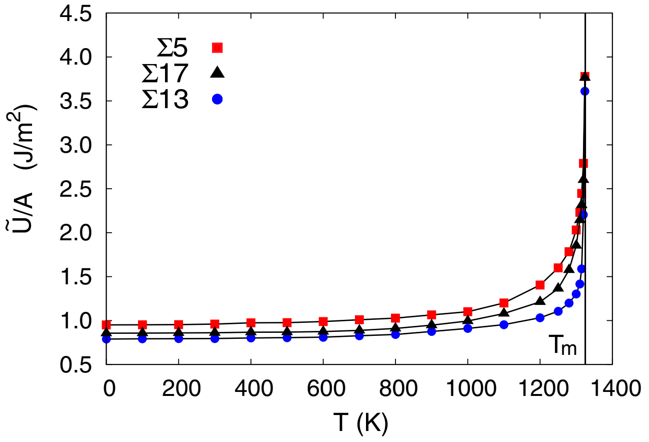

FIG. 14. Excess energy per unit area, $\tilde{U}/A$, as a function of temperature for three GBs in pure Cu. The vertical line indicates the bulk melting point.

As a consistency check, the analytical disjoining potentials obtained by the fitting were inserted in Eq. (20) and the width probability distributions were normalized to unity by numerical integration. The probability distributions obtained are shown by solid curves in Figs. 8, 10, and 12. At temperatures close to the melting point, these curves reproduce the individual distributions quite well. At larger undercoolings, the agreement becomes less accurate, which is not surprising given that the GBs become nearly dry and their description as a liquid layer is a crude approximation.

2. *Free energy of premelted grain boundaries*

The GB free energies were computed by thermodynamic integration. We used the integration scheme [70]

$$\gamma(T) = \frac{A_{\rm ref}T}{AT_{\rm ref}}\gamma_{\rm ref} + \frac{T}{A}\int_{T_{\rm ref}}^{T}\left(\sum_{i=1}^{2}\frac{A\tau_{ii}}{T}\frac{\partial e_{ii}}{\partial T} - \frac{\tilde{U}}{T^2}\right)dT, \tag{36}$$

where the excess energy $\tilde{U}$ and the interface stress τ_{ii} were discussed in Sec. III E. The quantities with index "ref" must be computed in the reference state. The term with the excess energy makes the leading contribution to the integral. Figure 14 shows the excess energy per unit GB area as a function of temperature. This energy remains nearly constant at low temperatures and sharply increases in the premelting region. It is interesting to note that the ranking of the GB energies at 0 K ($\gamma_{\Sigma 5} > \gamma_{\Sigma 17} > \gamma_{\Sigma 13}$) persists all the way to the melting point. This trend suggests that high/low energy GBs at 0 K are likely

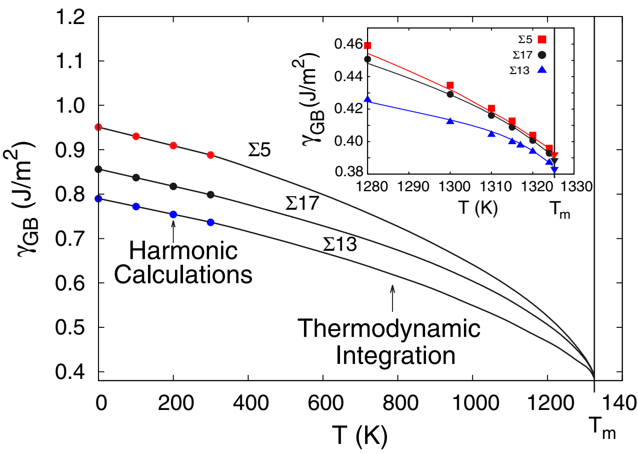

FIG. 15. GB free energy as a function of temperature for three GBs in pure Cu. The main plot shows the results of thermodynamic integration. The inset compares these results with predictions of the liquid layer model near the melting point (points).

to remain high/low energy boundaries at all temperatures. Accordingly, the 0-K GB energy can be a reasonably good predictor of premelting behavior. This correlation was also noted in the previous phase field studies on GB premelting [32]. The reference temperature T_{ref} was 300 K and the integration in Eq. (36) was carried out numerically.

The functions $\gamma(T)$ for the three GBs are plotted in Fig. 15. The plots include the GB energies at 0 K and the free energies at 100 and 200 K computed in the quasiharmonic approximation. These extra points demonstrate a smooth continuation of the curves below the temperature range 300 K $\leqslant T \leqslant$ 1324 K of thermodynamic integration. Although this method becomes less accurate as we deviate further away from the reference state, it was interesting to examine the values of γ at the bulk melting point. In the liquid layer model with a repulsive disjoining potential, these γ are expected to give $2\gamma_{SL}$. Thus γ_{SL} could be obtained by linear extrapolation of the plots from 1324 to 1325.25 K. Instead, we used a slightly more refined procedure explained below. The calculation gives the γ_{SL} values of 0.196, 0.194, and 0.192 J/m^2 for the Σ5, Σ17, and Σ13 GBs, respectively. These numbers refer to the solid-liquid interface orientations of (210), (320), and (520), respectively. The orientation dependence of γ_{SL} suggested by these numbers is small. All three numbers are in close agreement with $\gamma_{SL} = 0.199$ J/m^2 obtained in the previous work [48,71] for the (110) interface orientation using the same interatomic potential.

The GB free energy can also be calculated within the liquid layer model using the analytical disjoining potentials $\Psi(w)$ and the normalized width probability distributions $P(w)$. Note that thermodynamic integration naturally includes the effect of GB width fluctuations. Thus the quantity that should be compared with the results of thermodynamic integration is the GB free energy $\bar{\gamma}$ averaged over the width distribution. This quantity is defined by Eq. (22) with $\bar{w}$ and $\overline{\Psi(w)}$ given by Eqs. (23) and (24). The integrals in these equations were computed numerically.

The following procedure was then applied. We postulate that at the last point sampled (1324 K), $\bar{\gamma}$ matches γ obtained by thermodynamic integration. From this condition, we obtain

$$\gamma_{SL} = \tfrac{1}{2}\left(\gamma - \overline{\Psi(w)} + p_d^0 \bar{w}\right), \tag{37}$$

where $\bar{w}$ and $\overline{\Psi(w)}$ were computed at the last point. The values of γ_{SL} obtained by this procedure were quoted in the previous paragraph. Using these values of γ_{SL}, the entire function $\bar{\gamma}(T)$ was calculated from Eq. (22). The inset in Fig. 15 compares the GB free energies computed by the two methods. Given that the two calculations are independent (except for forcing their match at 1324 K), the agreement is very good. This lends additional credence to the liquid layer model at premelting temperatures. At lower temperatures, the comparison becomes impossible since the width probability distributions could not be extracted from the simulations and the liquid layer model is not expected to be valid.

B. Grain boundary premelting in Cu-Ag solutions

1. Premelting behavior and disjoining potentials

As the grain composition c approaches the solidus line, the amount of GB segregation of Ag rapidly increases (Fig. 16). The segregation zone grows wider and the atomic positions within this zone become increasingly disordered. At the undersaturation of $\Delta c = -0.11$ at.%Ag, the Σ5 GB becomes essentially a layer of the Cu-Ag liquid solution.

This trend is quantified in Fig. 17 where the average GB width $\bar{w}$ is plotted against ΔM for all three GBs. Each GB becomes wider with increasing temperature at a fixed ΔM or with decreasing $|\Delta M|$ at a fixed temperature. At fixed T and ΔM, the GB width decreases in the order Σ5, Σ17, and Σ13. While the widths of the Σ5 and Σ17 GBs diverge to infinity when approaching the solidus line, the Σ13 GB retains a finite width at the solidus line. In this case, it was possible to oversaturate the grains beyond the solidus line. In such oversaturated states, the GB width still remained finite until some point at which the entire system abruptly melted.

The disjoining potentials were extracted from the width probability distributions computed by the methodology discussed in Secs. III C and III D and illustrated in Figs. 7 and 8. For the Σ5 GB, $\Psi(w)$ remains repulsive at all points along the solidus (Fig. 18). Although the changes in the shape of the disjoining potential are small, there is a trend for it to shift towards smaller GB widths and develop a shoulder at around 1.5–2 nm as the temperature decreases.

By contrast, the disjoining potential of the Σ17 GB varies with temperature more dramatically (Fig. 19). As temperature decreases along the solidus line, the initially repulsive disjoining potential of pure Cu gradually transitions to the intermediate shape discussed in Sec. II D [cf. Fig. 3(a)]. The shoulder on the curve flattens at 1000 K and develops a double-well shape with a shallow minimum at $w \approx$ 1.3 nm. This shape evolution originates from the emergence of a second maximum in the width probability distribution as illustrated in Fig. 20. It should be mentioned that, due to the low temperature and complex shape of the distributions, these calculations required the longest simulation runs of all that

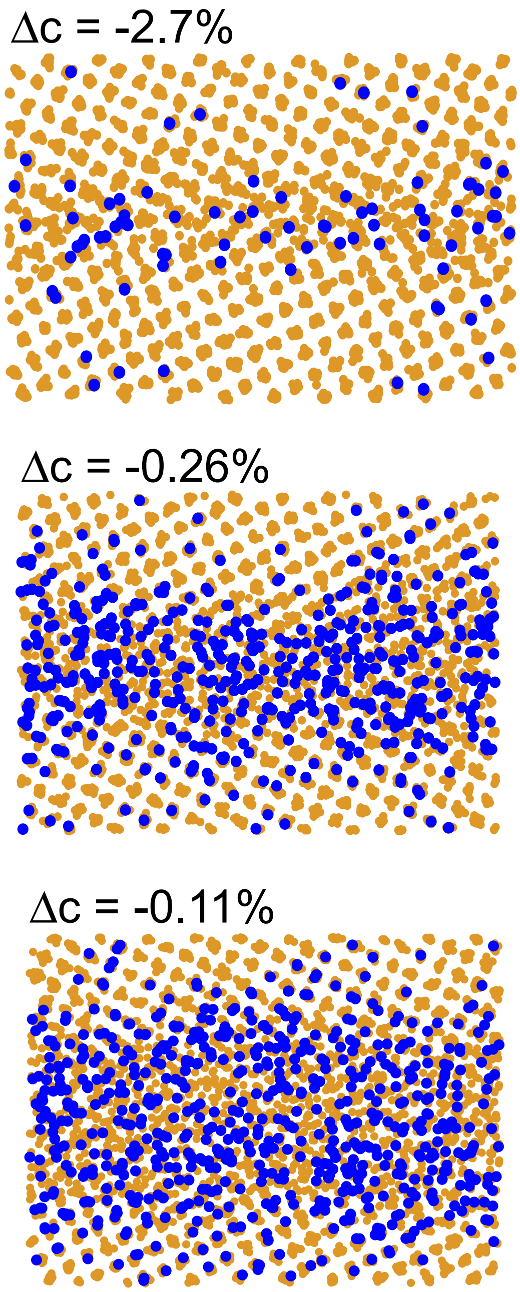

FIG. 16. Premelted structures of the $\Sigma 5$ GB at the temperature of 1100 K at different undersaturations Δc (at.%Ag). The atomic positions are projected along the [001] tilt axis normal to the page, with yellow points representing Cu atoms and blue points Ag atoms.

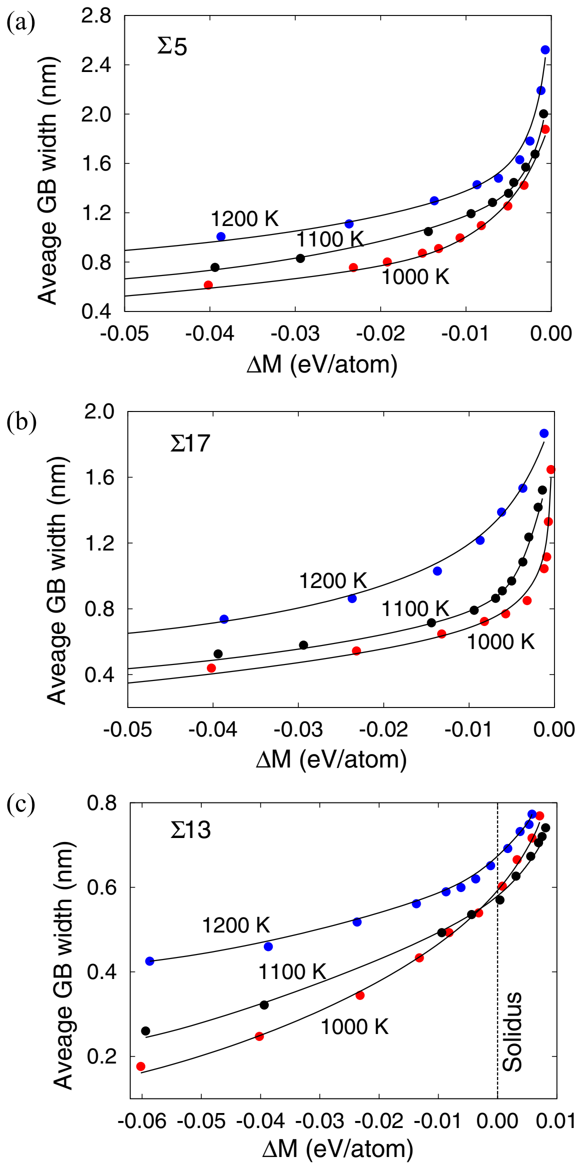

FIG. 17. Average width of the (a) $\Sigma 5$, (b) $\Sigma 17$ and (c) $\Sigma 13$ GBs in Cu-Ag solid solutions as a function of the diffusion potential ΔM relative the solidus line. The points represent individual simulations. The solid lines are Bezier curves intended to show the trends.

were implemented in this work.[9] The results are still subject to larger statistical errors than for single-peak distributions. At $\Delta M = -0.0032$ eV, the distribution does have a single peak. However, as we approach closer to the solidus line ($\Delta M \geqslant -0.0012$ eV), a second peak emerges and grows higher until we reach the last point closest to the solidus ($\Delta M = -0.0004$ eV) at which the second peak is higher than the first.

Because of the importance of the bimodal distributions as evidence of the intermediate disjoining potential, special care was taken to ensure that the bimodality is not an artifact and to understand its origin. Figure 21 shows a typical fragment of the simulation for the $\Sigma 17$ GB at 1000 K for one of the grain compositions showing the bimodality. The plot clearly shows that the boundary spontaneously switches back and forth between two states, with a smaller and a larger average width. One of the two states is stable while the other metastable. It is

---

[9] To obtain additional statistics for the bimodal distributions, the MC simulations were run four times longer than for unimodal distributions. The segments of the disjoining potential had significant overlaps where they did not match as smoothly as for unimodal distributions. Nevertheless, the existence of two peaks and thus the oscillatory region of the disjoining potential at 1000 K (Fig. 19) are beyond reasonable doubts.

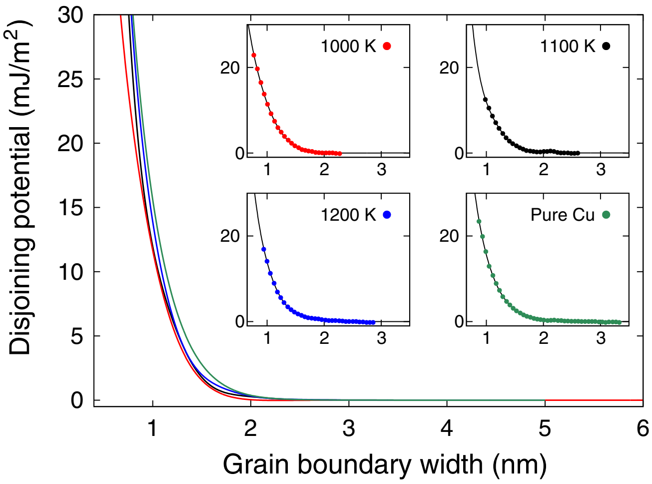

FIG. 18. Disjoining potentials for the Σ5 GB in the Cu-Ag solid solution at the three different temperatures and in pure Cu. The insets show the fits of the simulation results (points) by the analytical function $\Psi(w)$ (curves). The main plot summarizes the fitted functions.

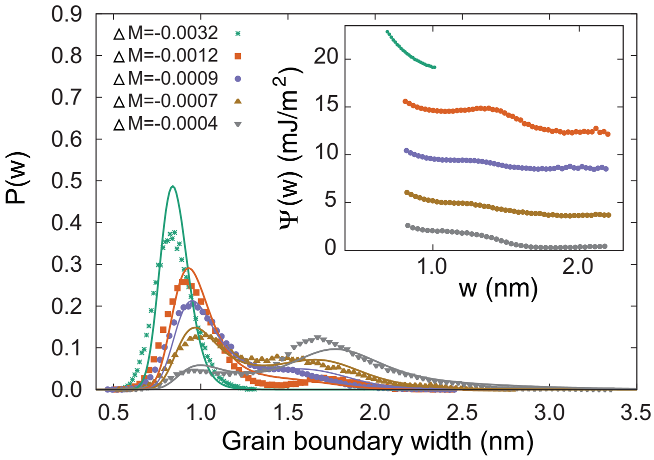

FIG. 20. Probability density functions for different values of ΔM (in eV) computed for the Σ17 GB at the temperature of 1000 K. The points represent the original histograms while the curves are the normalized distributions predicted by the analytical disjoining potential. The inset shows segments of the disjoining potential obtained by inversion of individual probability functions.

the existence of these two states that gives rise to the two peaks in the GB width distribution $P(w)$. The relative heights of the peaks bear information about the relative stability of the two states. Thus the rise of the peak corresponding to the wider GB state indicates that this GB state becomes increasingly more stable as we approach the solidus line, and eventually becomes more stable than the narrower state. Therefore we can expect that a thin-to-thick transition occurs between the two states at some value of ΔM. As discussed in Sec. II D, this transition arises due to the intermediate shape of the disjoining potential.

Finally, the disjoining potential of the Σ13 GB evolves from repulsive to attractive as temperature decreases along the solidus line (Fig. 22). In pure Cu, the potential curve is only beginning to develop a shoulder but remains monotonically decreasing with w (cf. Fig. 13). Accordingly, the boundary premelts continuously when approaching T_m and can be described by the liquid layer model satisfactorily (although not as accurately as for the two other GBs). As the potential evolves to attractive, the GB width becomes relatively small (<1 nm) and its description as a liquid layer becomes a crude approximation. Nevertheless, the simulation results show unambiguously that the disjoining potential is attractive. The boundary retains a finite width along the solidus line until close to pure Cu and can be oversaturated beyond the solidus line. The shapes of the curves in Fig. 22 suggest that $\Psi(w)$ must

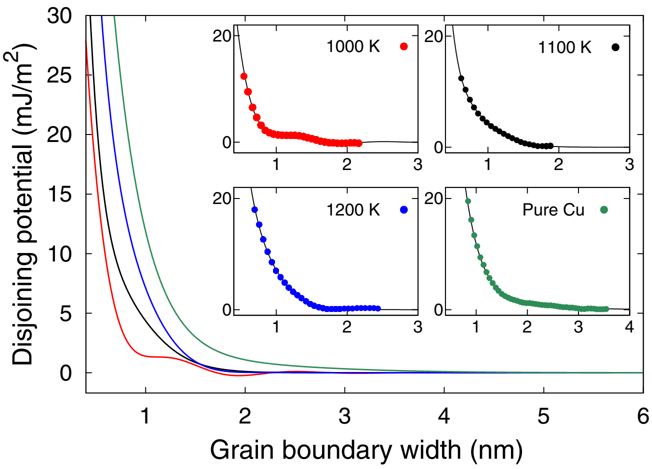

FIG. 19. Disjoining potentials for the Σ17 GB in the Cu-Ag solid solution at the three different temperatures and in pure Cu. The insets show the fits of the simulation results (points) by the analytical function $\Psi(w)$ (curves). The main plot summarizes the fitted functions. Note the transition of the disjoining potential from repulsive to intermediate with decreasing temperature.

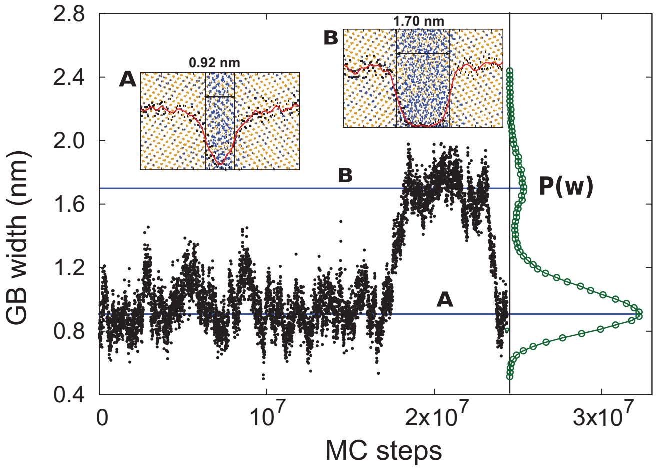

FIG. 21. A typical fragment of MC simulations for the Σ17 GB at 1000 K with undersaturation $\Delta M = -0.0012$ eV. The GB spontaneously switches between two states, labeled A and B, with different widths. Multiple repetitions of such switches produce two peaks in the width probability distribution $P(w)$. The insets show order parameter profiles in snapshots drawn from the two states. The GB widths in the snapshots are indicated.

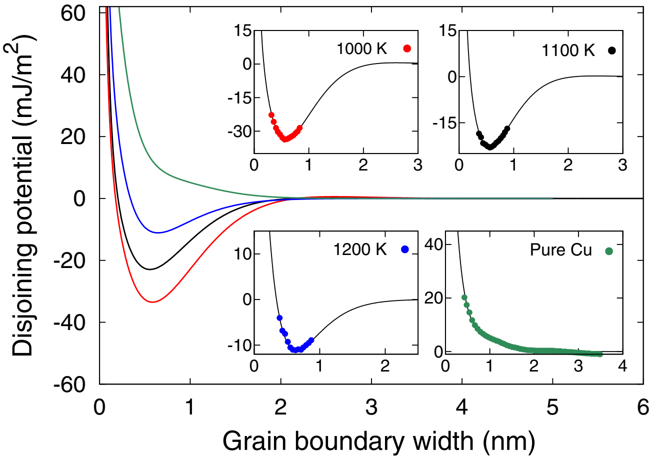

FIG. 22. Disjoining potentials for the $\Sigma 13$ GB in the Cu-Ag solid solution at the three different temperatures and in pure Cu. The insets show the fits of the simulation results (points) by the analytical function $\Psi(w)$ (curves). The main plot summarizes the fitted functions.

become intermediate at temperatures between 1200 K and T_m, but a study of this temperature interval was not pursued in this work.

2. *Chemical composition of grain boundaries*

When a GB becomes a liquid layer, its chemical composition is expected to approach the liquidus composition c_L^* as the grains approach the solidus composition c_S^* at the same temperature. In the previous MC study of the $\Sigma 5$ GB [28], this trend was indeed followed within the statistical scatter of the data. The present simulations offer the opportunity of a more accurate test of this trend for the $\Sigma 5$ and $\Sigma 17$ GBs (we excluded the $\Sigma 13$ GB for which the notion of a liquid layer is not well-defined).

Figure 23 shows the chemical composition, $c_{\rm GB}$, at the center of the GB region as a function of ΔM. To find $c_{\rm GB}$, the bounds z_1 and z_2 of the GB region were calculated from the order parameter profile in each snapshot as illustrated in Fig. 7. The GB center was defined by $z_c = (z_1 + z_2)/2$ and its chemical composition $c_{\rm GB}$ was computed by averaging over a 0.1 nm window centered at z_c. Each point shown in Fig. 23 was obtained by averaging $c_{\rm GB}$ over all snapshots saved in the simulation. We observe that at high temperatures, $c_{\rm GB}$ increases monotonically with ΔM and reaches the liquidus composition c_L^* as the grains reach the solidus line ($\Delta M \rightarrow 0$). We also see that, at a given ΔM, $c_{\rm GB}$ increases with decreasing temperature. In other words, the GB segregation becomes stronger at low temperatures, suggesting a negative segregation energy (binding of Ag to the GBs). It is interesting to note, however, that at low temperatures, $c_{\rm GB}$ overshoots c_L^* before turning over and returning to c_L^* from above. Furthermore, at least for the $\Sigma 5$ GB at 1100 K, the overshoot is followed by a slight undershoot before $c_{\rm GB}$ reaches c_L^*. These subtle but important effects could not be resolved in the previous work [28], nor were they seen in the phase field simulations [32].

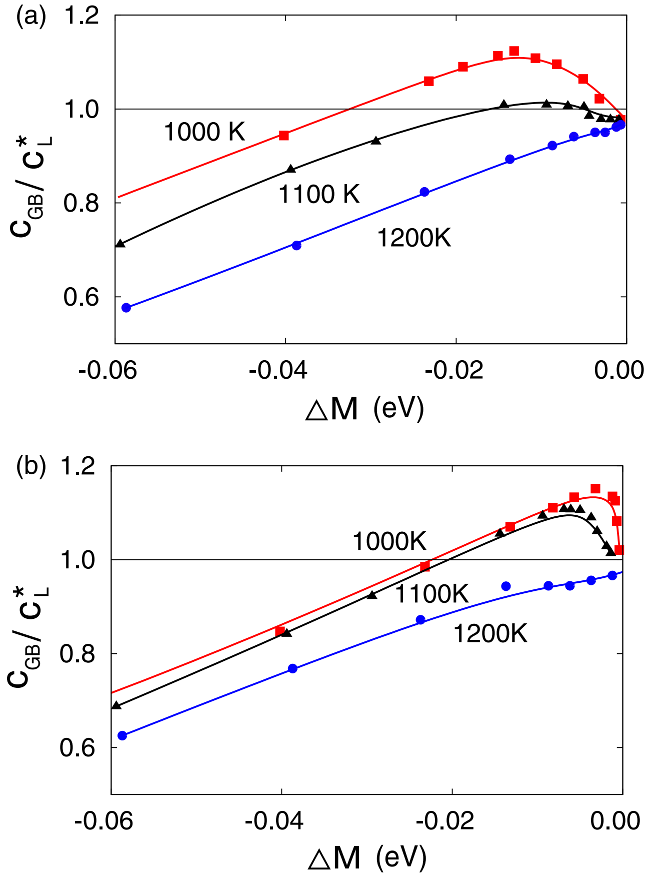

FIG. 23. Chemical composition $c_{\rm GB}$ at the center of the GB region normalized by the liquidus composition c_L^* as a function of undersaturation ΔM. The lines are Bezier curves intended to highlight the trends.

For a more detailed understanding of these effects, we examined the local chemical composition profiles across the GBs. To obtain them, the GB center z_c was found in each snapshot and the entire simulation block was translated to bring this point to $z = 0$. This re-centering procedure was applied to all snapshots saved in the simulation. A set of thin layers parallel to the GB plane was then constructed and the chemical composition of each layer was averaged over all snapshots. The discrete composition profile obtained was thus centered at $z = 0$. It was then represented by a continuous profile by linear interpolation between the bin centers.

Examples of composition profiles are shown in Fig. 24 for the $\Sigma 5$ GB at 1000 K for a set of ΔM values near the solidus (similar profiles were also generated for the $\Sigma 17$ and $\Sigma 13$ GBs with similar results). At early stages of premelting, the profile has a single maximum whose height increases as we move closer to the solidus line. At some point, the maximum overshoots the liquidus composition. Then, instead of growing higher, the peak begins to widen, forms a plateau, and then splits into two local maxima on either side of a local minimum forming at $z = 0$. The composition at this minimum decreases and becomes slightly below c_L^*. Although it was not possible in this work to probe the states even closer to the solidus, we expect that $c_{\rm GB}$ later increases and

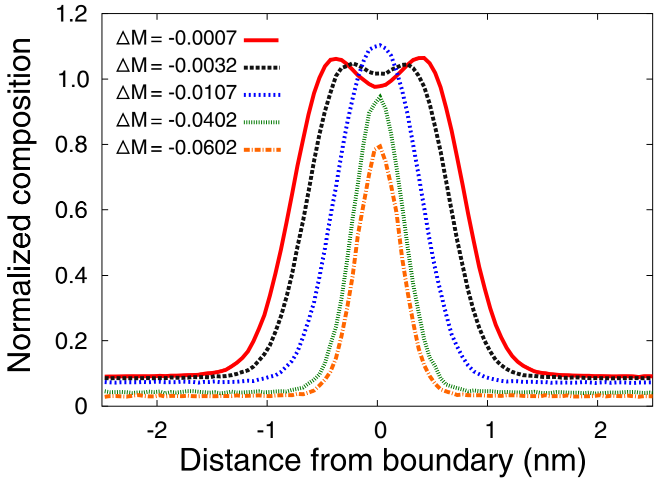

FIG. 24. Chemical compositional profiles (normalized by the liquidus composition c_L^*) across the Σ5 GB for different undersaturations ΔM (eV) at the temperature of 1000 K.

eventually approaches c_L^* as the grain composition reaches the solidus line. This evolution of the composition profiles is consistent with the formation of two solid-liquid interfaces bounding a liquid layer. The two maxima are associated with the principal peaks of the compositional oscillations created by the solid-liquid interfaces (cf. Fig. 4), whereas the minimum in between is a superposition of the depletion zones existing next to the principal peaks. This superposition can explain the slight undershoot of c_{GB} (Figs. 23 and 24). When the GB is narrow, the principal peaks merge into a single peak and amplify each other, giving rise to the compositional overshoot discussed above.

The chemical composition of the GBs can also be characterized by the total amount of segregation, $\tilde{N}_2/A$, per unit GB area. Examples of the computed segregation isotherms are shown in Fig. 25. The isotherms remain nearly linear until the grain composition approaches the solidus line, at which point the segregation rapidly accelerates and diverges to infinity. This behavior closely correlates with the divergence of the GB width (Fig. 17), which is expected given that the composition inside the GB becomes nearly constant (and close to the liquidus composition) and therefore $\tilde{N}_2/A \propto w$.

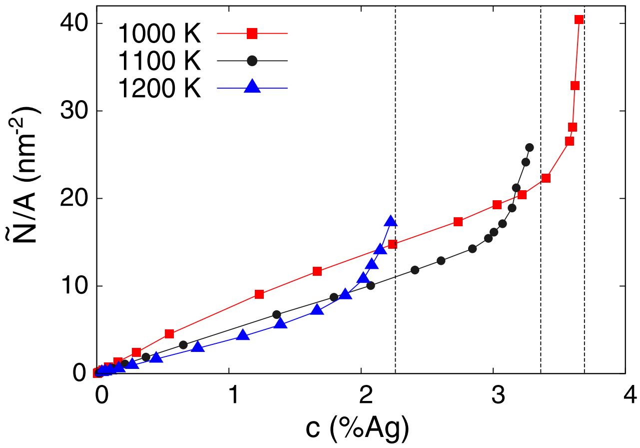

FIG. 25. Segregation isotherms for the Σ17 GB at three temperatures. The vertical dashed lines mark the solidus compositions c_S^*.

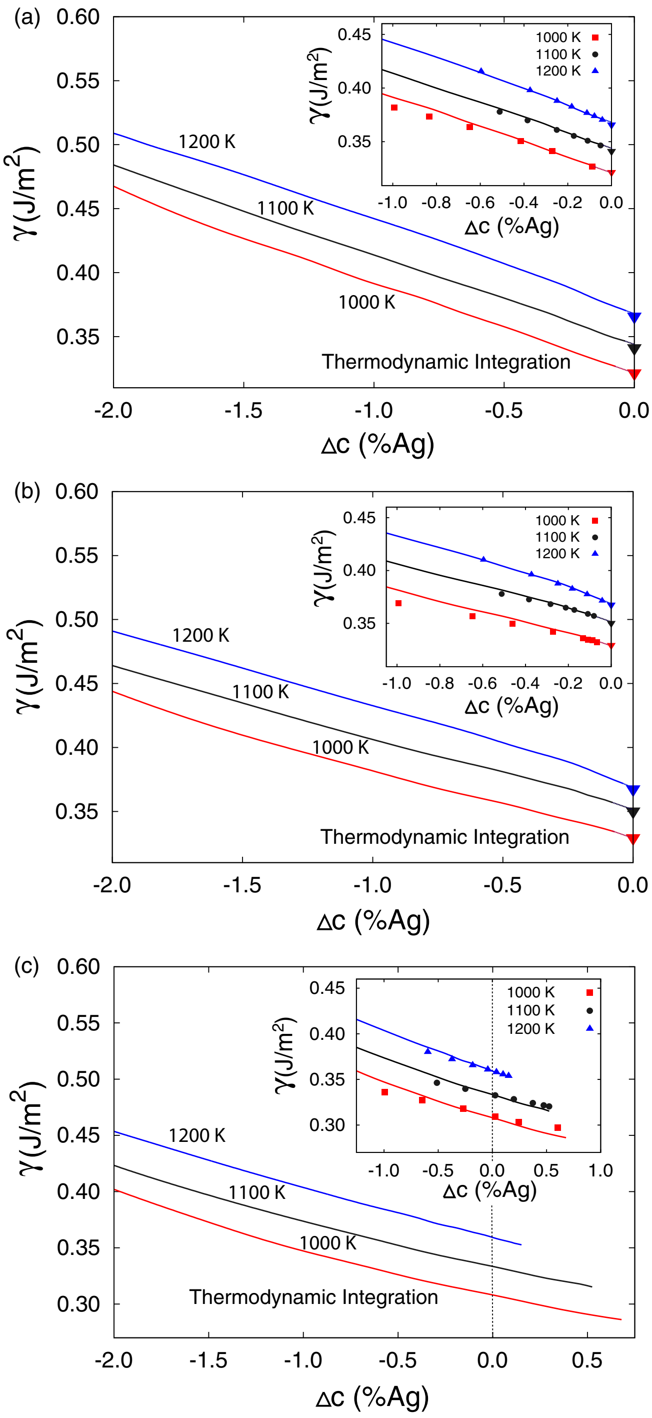

FIG. 26. Free energy of the (a) Σ5, (b) Σ17, and (c) Σ13 GBs in the Cu-Ag solution at the three temperatures sampled. The solid lines in the main plot were obtained by thermodynamic integration. The dotted lines are linear interpolations to the solidus line ($\Delta c = 0$). The inset compares these results with predictions of the liquid layer model (points) near the solidus.

3. Free energy of premelted grain boundaries

To compute the GB free energies, we applied the thermodynamic integration scheme based on the equation [70]

$$\gamma(c) = \frac{A_p}{A}\gamma_p + \int_0^c \left[-\frac{\tilde{N}_2}{A}\left(\frac{dM}{dc}\right)_T + \sum_{i=1}^{2} \tau_{ii}\left(\frac{de_{ii}}{dc}\right)_T \right] dc, \quad \text{fixed } T. \qquad (38)$$

(The original equation [70] has been modified by changing the integration variable from M to c.) Here, γ_p and A_p are the free energy and cross-sectional area of the GB in the pure Cu state ($c = 0$), which are known from the calculations reported in Sec. IV A 2. The properties appearing in the integrand were discussed in Sec. III E. The segregation term plays the dominant role while the interface stress term makes a small correction. The integration in Eq. (38) was performed numerically.

The functions $\gamma(c)$ are shown in Fig. 26 for all three GBs. At a fixed temperature, γ decreases with the solute concentration in the grains, which is consistent with the Gibbs adsorption equation given that the solute segregation is positive ($\tilde{N}_2 > 0$) and $(dM/dc)_T > 0$. Similar to the pure Cu case, γ_{SL} values were computed for the $\Sigma 5$ and $\Sigma 17$ GBs by applying Eq. (37) at the point closest to the solidus line. The calculations give the values of 0.161, 0.171, and 0.183 J/m^2 for the $\Sigma 5$ GB and 0.165, 0.175, and 0.184 J/m^2 for the $\Sigma 17$ GB at the temperatures of 1000, 1100, and 1200 K, respectively. These numbers are in good agreement with previous calculations (by a different method) for a solid-liquid interface with the (110) orientation [48], which gave the free energies of 0.177, 0.184, and 0.190 J/m^2 at the respective temperatures. A more detailed comparison is shown in Fig. 27. It is difficult to separate calculation errors from the intrinsic orientation dependence of γ_{SL}. Nevertheless, all calculations indicate that γ_{SL} increases with temperature along the solidus line. This consistency of the results further validates the present methodology. For the sake of completeness, Fig. 27 also includes γ_{SL} values obtained by formally applying the same procedure to the $\Sigma 13$ GB (0.172, 0.178, and 0.185 J/m^2 at the temperatures of 1000, 1100, and 1200 K, respectively). Surprisingly, the results are consisted with those for the truly premelted GBs, even though this boundary can hardly be represented by a liquid layer. This agreement could be partially fortuitous.

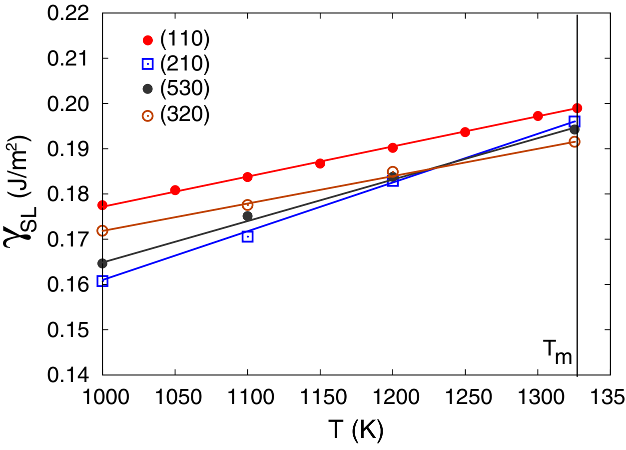

FIG. 27. Solid-liquid interface free energies in the Cu-Ag system computed in this work from GB premelting simulations. The interface planes are indicated in the legends. For comparison, the plot includes γ_{SL} of the (110) interface computed in previous work [48].

Figure 26 also compares the GB free energies γ from thermodynamic integration with calculations of $\bar{\gamma}$ in the framework of the liquid layer model [Eqs. (22)–(24)]. Recall that γ and $\bar{\gamma}$ are forced to coincidence at the last point of the simulations before the solidus, but all other points are results of independent calculations. Note the good agreement between the two calculations, especially at 1200 K.

V. CONCLUSIONS

The proposed analytical form of the disjoining potential describes repulsive, attractive and intermediate interactions between solid-liquid interfaces by a single equation. In contrast to the previously used exponential potentials, Eq. (26) captures two physical effects. First, the potential can reproduce two (or more) local minima of the GB free energy and thus stable and metastable GB states separated by a barrier. This, in turn, leads to first order thin-to-thick phase transitions in premelted GBs. Such transitions give rise to GB phase equilibrium lines on bulk phase diagrams that end at a critical point. Such lines were predicted in previous phase field simulations [30–32]. Second, the potential has an oscillating tail. These oscillations are strongly damped and reflect the existence of spatial oscillations of chemical composition at solid-liquid interfaces (see, e.g., Fig. 4). Superposition of these compositional oscillations is expected to produce oscillations of the attraction forces between interfaces. Furthermore, these oscillations might, in principle, produce a whole cascade of thin-to-thick transitions similar to the layering transitions in surface adsorption. Future work may explore if the monolayer, double-layer and other segregation patterns in alloy GBs [75,76] (often referred to as different "complexions") [7] can also be described by disjoining potentials with oscillating tails.

The atomistic simulations of GBs in binary Cu-Ag solutions conducted in this work have explored various temperatures, chemical compositions and GB energies. The fluctuation approach applied previously to single-component GBs [24,25] and extended here to binary systems, was applied to extract the disjoining potentials from the simulations under various conditions. All three types of disjoining potentials were found—repulsive, attractive, and intermediate—in full agreement with predictions of the liquid layer model with the analytical potential. Multiple consistency checks performed during the simulations demonstrate the reliability of the results. In particular, the GB free energy was computed by thermodynamic integration, producing results consistent with the liquid layer model with the analytical disjoining potential. Calculations of solid-liquid interface free energies also gave consistent results for different GBs and are in agreement with previous calculations by independent methods.

An important result of the simulations is the confirmation of the existence of multiple stable and metastable states of premelted GBs under appropriate conditions. Such states are characterized by different GB widths as well as other excess properties. During continuous variations of thermodynamic state of the grains, the relative stability of such states varies and at some point can result in a thin-thick phase coexistence. Additional calculations could generate a thin-thick phase coexistence line on the Cu-Ag phase diagram, but this is left for future work.

ACKNOWLEDGMENTS

We are grateful to V. Yamakov (NASA) for developing the parallel Monte Carlo code used in this work. This research was supported by the National Science Foundation, Division of Materials Research, the Metals and Metallic Nanostructures Program, Award No. 1308667.

---

[1] A. P. Sutton and R. W. Balluffi, *Interfaces in Crystalline Materials* (Clarendon Press, Oxford, 1995).

[2] Y. Mishin, M. Asta, and J. Li, Atomistic modeling of interfaces and their impact on microstructure and properties, Acta Mater. **58**, 1117 (2010).

[3] R. W. Balluffi and R. Maurer, On rotating sphere-on-plate experiments and the question of whether high angle grain boundaries melt below bulk meting temperatures, Scripta Metall. **22**, 709 (1988).

[4] T. E. Hsieh and R. W. Balluffi, Experimental study of grain boundary melting in aluminum, Acta Metall. **37**, 1637 (1989).

[5] J. Luo, V. K. Gupta, D. H. Yoon, and H. M. Meyer, Segregation-induced grain boundary premelting in nickel-doped tungsten, Appl. Phys. Lett. **87**, 231902 (2005).

[6] V. K. Gupta, D. H. Yoon, H. M. Meyer, and J. Luo, Thin intergranular films and solid-state activated sintering in nickel-doped tungsten, Acta Mater. **55**, 3131 (2007).

[7] P. R. Cantwell, M. Tang, S. J. Dillon, J. Luo, G. S. Rohrer, and M. P. Harmer, Grain boundary complexions, Acta Mater. **62**, 1 (2013).

[8] R. A. Masumura, M. E. Glicksman, and C. L. Vold, Absolute solid-liquid and grain boundary energies of bismuth, Scripta Metall. **6**, 943 (1972).

[9] C. L. Vold and M. E. Glicksman, Behavior of grain boundaries near the melting point, in H. Hu, editor, *The Nature and Behavior of Grain Boundaries* (Metallurgical Society of AIME, Plenum Press, New York, 1972), pp. 171–183.

[10] T. Watanabe, S. I. Kimura, and S. Karashima, The effect of grain boundary structural transformation on sliding in (1010)-tilt zinc bicrystals, Philos. Mag. A **49**, 845 (1984).

[11] F. Inoko, T. Okada, T. Muraga, Y. Nakano, and T. Yoshikawa, Strain induced grain boundary premelting in bulk copper bicrystals, Interface Sci. **4**, 263 (1997).

[12] G. Gottstein, D. A. Molodov, and L. S. Shvindlerman, Grain boundary migration in metals: Recent developments, Interface Sci. **6**, 7 (1998).

[13] S. V. Divinski, M. Lohman, C. Herzig, B. Straumal, B. Baretzky, and W. Gust, Grain-boundary melting phase transition in the Cu-Bi system, Phys. Rev. B **71**, 104104 (2005).

[14] G. Ciccotti, M. Guillope, and V. Pontikis, High-angle grain-boundary transition: A molecular-dynamics study, Phys. Rev. B **27**, 5576 (1983).

[15] M. Guillope, G. Ciccotti, and V. Pontikis, Relation between intergranular diffusion and structure: A molecular dynamics study, Surf. Sci. **144**, 67 (1984).

[16] J. Q. Broughton and G. H. Gilmer, Thermodynamic Criteria for Grain Boundary Melting: A Molecular-Dynamics Study, Phys. Rev. Lett. **56**, 2692 (1986).

[17] J. F. Lutsko, D. Wolf, S. R. Phillpot, and S. Yip, Molecular-dynamics study of lattice-defect-nucleated melting in metals using an embedded-atom-method potential, Phys. Rev. B **40**, 2841 (1989).

[18] J. F. Lutsko, D. Wolf, S. Yip, S. R. Phillpot, and T. Nguyen, Molecular-dynamics method for the simulation of bulk-solid interfaces at high temperatures, Phys. Rev. B **38**, 11572 (1988).

[19] T. Nguyen, P. S. Ho, T. Kwok, C. Nitta, and S. Yip, Thermal structural disorder and melting at a crystalline interface, Phys. Rev. B **46**, 6050 (1992).

[20] J. Lu and J. A. Szpunar, Molecular dynamics simulation of a twist $\Sigma = 5$ grain boundary, Interface Sci. **3**, 143 (1995).

[21] J. Q. Broughton and G. H. Gilmer, Grain-boundary shearing as a test for interface melting, Modelling Simul. Mater. Sci. Eng. **6**, 87 (1998).

[22] P. Keblinski, D. Wolf, S. R. Phillpot, and H. Gleiter, Self-diffusion in high-angle fcc metal grain boundaries by molecular dynamics simulations, Philos. Mag. A **79**, 2735 (1999).

[23] A. Suzuki and Y. Mishin, Atomic mechanisms of grain boundary diffusion: Low versus high temperatures, J. Mater. Sci. **40**, 3155 (2005).

[24] J. J. Hoyt, D. Olmsted, S. Jindal, M. Asta, and A. Karma, Method for computing short-range forces between solid-liquid interfaces driving grain boundary premelting, Phys. Rev. E **79**, 020601 (2009).

[25] S. J. Fensin, D. Olmsted, D. Buta, M. Asta, A. Karma, and J. J. Hoyt, Structural disjoining potential for grain-boundary premelting and grain coalescence from molecular-dynamics simulations, Phys. Rev. E **81**, 031601 (2010).

[26] G. Besold and O. G. Mouritsen, Grain-boundary melting: A Monte Carlo study, Phys. Rev. B **50**, 6573 (1994).

[27] G. Besold and O. G. Mouritsen, Competition between domain growth and interfacial melting, Comp. Mater. Sci. **18**, 225 (2000).

[28] P. L. Williams and Y. Mishin, Thermodynamics of grain boundary premelting in alloys. II. Atomistic simulation, Acta Mater. **57**, 3786 (2009).

[29] A. Lobkovsky and J. W. Warren, Phase field model of premelting of grain boundaries, Physica D **164**, 202 (2002).

[30] M. Tang, W. C. Carter, and R. M. Cannon, Diffuse interface model for structural transitions of grain boundaries, Phys. Rev. B **73**, 024102 (2006).

[31] M. Tang, W. C. Carter, and R. M. Cannon, Grain Boundary Transitions in Binary Alloys, Phys. Rev. Lett. **97**, 075502 (2006).

[32] Y. Mishin, W. J. Boettinger, J. A. Warren, and G. B. McFadden, Thermodynamics of grain boundary premelting in alloys. I. Phase field modeling, Acta Mater. **57**, 3771 (2009).

[33] N. Wang, R. Spatschek, and A. Karma, Multi-phase-field analysis of short-range forces between diffuse interfaces, Phys. Rev. E **81**, 051601 (2010).

[34] J. Berry, K. R. Elder, and M. Grant, Melting at dislocations and grain boundaries: A phase field crystal study, Phys. Rev. B **77**, 224114 (2008).

[35] J. Mellenthin, A. Karma, and M. Plapp, Phase-field crystal study of grain-boundary premelting, Phys. Rev. B **78**, 184110 (2008).

[36] R. Spatschek, A. Adland, and A. Karma, Structural short-range forces between solid-melt interfaces, Phys. Rev. B **87**, 024109 (2013).

[37] A. Adland, A. Karma, R. Spatschek, D. Buta, and M. Asta, Phase-field-crystal study of grain boundary premelting and shearing in bcc iron, Phys. Rev. B **87**, 024110 (2013).

[38] E. Rowan, The structural disjoining potential of grain boundary premelting in binary alloys using phase field crystal model, MS thesis, McMaster University, Hamilton, Ontario, Canada, 2013.

[39] L. L. Lu, T. T. Hu, G. M. Lu, and Z. Chen, Phase-field crystal study of segregation induced grain-boundary premelting in binary alloys, Physica B **451**, 128 (2014).

[40] E. Asadi and M. A. Zaeem, A review of quantitative phase-field crystal modeling of solid–liquid structures, JOM **67**, 186 (2015).

[41] R. Lipowsky, Melting at grain boundaries and surfaces, Phys. Rev. Lett. **57**, 2876 (1986).

[42] R. Lipowsky and M. E. Fisher, Scaling regimes and functional renormalization for wetting transitions, Phys. Rev. B **36**, 2126 (1987).

[43] G. Forgacs, R. Lipowsky, and T. M. Nieuwenhuizen, *The Behavior of Interfaces in Ordered and Disordered Systems*, edited by C. Domb and J. Lebowitz, Phase Transitions and Critical Phenomena (Academic Press, San Diego, 1991), Vol. 14, Chap. 2, pp. 135–364.

[44] M. Rappaz, A. Jacot, and W. J. Boettinger, Last-stage solidification of alloys: Theoretical model of dendrite-arm and grain coalescence, Metall. Mater. Trans. A **34**, 467 (2003).

[45] R. Pandit, M. Schick, and M. Wortis, Systematics of multilayer adsorption phenomena on attractive substrates, Phys. Rev. B **26**, 5112 (1982).

[46] Y. Mishin, Thermodynamic theory of equilibrium fluctuations, Ann. Phys. **363**, 48 (2015).

[47] F. C. Larché and J. W. Cahn, The interactions of composition and stress in crystalline solids, Acta Metall. **33**, 331 (1985).

[48] T. Frolov and Y. Mishin, Solid-liquid interface free energy in binary systems: Theory and atomistic calculations for the (110) Cu-Ag interface, J. Chem. Phys. **131**, 054702 (2009).

[49] J. W. Cahn, *Thermodynamics of Solid and Fluid Surfaces*, edited by W. C. Johnson and J. M. Blackely, Interface Segregation (American Society of Metals, Metals Park, OH, 1979), Chap. 1, pp. 3–23.

[50] S. H. Oh, Y. Kauffmann, C. Scheu, W. D. Kaplan, and M. Ruhle, Ordered liquid aluminum at the interface with sapphire, Science **310**, 661 (2005).

[51] W. D. Kaplan and Y. Kauffmann, Structural order in liquids induced by interfaces with crystals, Annu. Rev. Mater. Res. **36**, 1 (2006).

[52] M. Baram, D. Chatain, and W. D. Kaplan, Nanometer-thick equilibrium films: The interface between thermodynamics and atomistics, Science **332**, 206 (2011).

[53] A. Hashibon, J. Adler, M. W. Finnis, and W. D. Kaplan, Ordering at solid-liquid interfaces between dissimilar materials, Interface Sci. **9**, 175 (2001).

[54] A. Hashibon, J. Adler, M. W. Finnis, and W. D. Kaplan, Atomistic study of structural correlations at a liquid-solid interface, Comput. Mat. Sci. **24**, 443 (2002).

[55] J. P. Palafox-Hernandez, B. B. Laird, and M. Asta, Atomistic characterization of the Cu–Pb solid–liquid interface, Acta Mater. **59**, 3137 (2011).

[56] M. S. Daw and M. I. Baskes, Embedded-atom method: Derivation and application to impurities, surfaces, and other defects in metals, Phys. Rev. B **29**, 6443 (1984).

[57] P. L. Williams, Y. Mishin, and J. C. Hamilton, An embedded-atom potential for the Cu-Ag system, Modelling Simul. Mater. Sci. Eng. **14**, 817 (2006).

[58] G. P. Purja Pun, V. Yamakov, and Y. Mishin, Interatomic potential for the ternary Ni–Al–Co system and application to atomistic modeling of the B2–L1_0 martensitic transformation, Model. Simul. Mater. Sci. Eng. **23**, 065006 (2015).

[59] V. Yamakov, J. D. Hochhalter, W. P. Leser, J. E. Warner, J. A. Newman, G. P. Purja Pun, Y. Mishin, Multiscale modeling of sensory properties of Co–Ni–Al shape memory particles embedded in an Al metal matrix, J. Mater. Sci. **51**, 1204 (2016).

[60] D. Frenkel and B. Smit, *Understanding Molecular Simulation: from Algorithms to Applications*, 2nd ed. (Academic, San Diego, 2002).

[61] D. P. Landau and K. Binder, *A Guide to Monte Carlo Simulations in Statistical Physics*, 3rd ed. (Cambridge University Press, Cambridge, 2009).

[62] J. A. Brown and Y. Mishin, Effect of surface stress on Ni segregatin in (110) NiAl thin films, Phys. Rev. B **69**, 195407 (2004).

[63] J. A. Brown and Y. Mishin, Segregation and structural transformations at Σ3 grain boundaries in NiAl: A Monte Carlo study, Acta Mater. **53**, 2149 (2005).

[64] Y. Mishin, Calculation of the γ/γ' interface free energy in the Ni-Al system by the capillary fluctuation method, Modeling Simul. Mater. Sci. Eng. **22**, 045001 (2014).

[65] B. Sadigh, P. Erhart, A. Stukowski, A. Caro, E. Martinez, and L. Zepeda-Ruiz, Scalable parallel Monte Carlo algorithm for atomistic simulations of precipitation in alloys, Phys. Rev. B **85**, 184203 (2012).

[66] A. Suzuki and Y. Mishin, Atomistic modeling of point defects and diffusion in copper grain boundaries, Interface Science **11**, 131 (2003).

[67] J. W. Cahn, Y. Mishin, and A. Suzuki, Coupling grain boundary motion to shear deformation, Acta Mater. **54**, 4953 (2006).

[68] J. W. Cahn, Y. Mishin, and A. Suzuki, Duality of dislocation content of grain boundaries, Philos. Mag. **86**, 3965 (2006).

[69] T. Frolov and Y. Mishin, Thermodynamics of coherent interfaces under mechanical stresses. I. Theory, Phys. Rev. B **85**, 224106 (2012).

[70] T. Frolov and Y. Mishin, Thermodynamics of coherent interfaces under mechanical stresses. II. Application to atomistic simulation of grain boundaries, Phys. Rev. B **85**, 224107 (2012).

[71] T. Frolov and Y. Mishin, Temperature dependence of the surface free energy and surface stress: and atomistic calculation for Cu (110), Phys. Rev. B **79**, 045430 (2009).

[72] T. Frolov and Y. Mishin, Orientation dependence of the solid–liquid interface stress: atomistic calculations for copper, Model. Simul. Mater. Sci. Eng. **18**, 074003 (2010).

[73] T. Frolov and Y. Mishin, Effect of nonhydrostatic stresses on solid-fluid equilibrium. II. Interface thermodynamics, Phys. Rev. B **82**, 174114 (2010).

[74] S. M. Foiles, Evaluation of harmonic methods for calculating the free energy of defects in solids, Phys. Rev. B **49**, 14930 (1994).

[75] T. Frolov, S. V. Divinski, M. Asta, and Y. Mishin, Effect of Interface Phase Transformations on Diffusion and Segregation in High-Angle Grain Boundaries, Phys. Rev. Lett. **110**, 255502 (2013).

[76] T. Frolov, M. Asta, and Y. Mishin, Segregation-induced phase transformations in grain boundaries, Phys. Rev. B **92**, 020103(R) (2015).